# Anisotropic error control for environmental applications*

L. Dedè[♯], S. Micheletti[♯], S. Perotto[♯]

30th October 2006

[♯] MOX– Modellistica e Calcolo Scientifico
Dipartimento di Matematica "F. Brioschi"
Politecnico di Milano
via Bonardi 9, 20133 Milano, Italy
{luca.dede,stefano.micheletti,simona.perotto}@mate.polimi.it

**Keywords**: Anisotropic mesh adaption; Goal-oriented analysis; Gradient recovery procedure; Advection-diffusion-reaction problems.

**AMS Subject Classification**: 65N30, 65N15, 65N50, 35J20, 76R99

**Abstract**

In this paper we aim at controlling physically meaningful quantities with emphasis on environmental applications. This is carried out by an efficient numerical procedure combining the goal-oriented framework [Acta Numer. 10 (2001) 1] with the anisotropic setting introduced in [Numer. Math. 89 (2001) 641]. A first attempt in this direction has been proposed in [Appl. Numer. Math. 51 (2004) 511]. Here we improve this analysis by carrying over to the goal-oriented framework the good property of the a posteriori error estimator to depend on the error itself, typical of the anisotropic residual based error analysis presented in [Comput. Methods Appl. Mech. Engrg. 195 (2006) 799; Numerical Mathematics and Advanced Applications - Enumath2001 Springer Verlag Italia (2003) 731]. On the one hand this dependence makes the estimator not immediately computable; nevertheless, after approximating this error via the Zienkiewicz-Zhu gradient recovery procedure [Internat. J. Numer. Methods Engrg. 24 (1987) 337; Internat. J. Numer. Methods Engrg. 33 (1992) 1331], the resulting estimator is expected to exhibit a higher convergence rate than the one in [Appl. Numer. Math. 51 (2004) 511]. As the broad numerical validation attests, the proposed estimator turns out to be more efficient in terms of d.o.f.'s per accuracy or equivalently, more accurate for a fixed number of elements.

*The research has been partly supported by the project COFIN 2005 *Numerical Modelling in Fluid Dynamics with Application to the Cardiovascular System and Environment.*

## 1 Introduction and motivations

In this work we aim at devising effective numerical techniques in view of environmental applications. For example we may be interested in studying the distribution of some pollutants in atmosphere or in water. This could be the case if one wants to measure the concentration of the pollutant (due to emissions by industrial plants or chimneys) in an observation area, e.g. a town, in order to keep it below a desired threshold, or if one desires to monitor the concentration of contaminants in a branch of a river caused, for instance, by industrial or agricultural waste material (see, e.g., [10]).
With a view to simulating such kind of phenomena one is led to monitoring or accurately computing quantities of interest, such as concentrations rather than fluxes in localized portions of the domain. Mathematically these quantities are identified by proper functionals, typically represented by interior or boundary integrals. The necessity to deal with physically meaningful quantities justifies the employment of a goal-oriented analysis. The basic feature of this approach consists of estimating, within a user-defined tolerance, the exact (but unknown) functional, evaluating the functional itself on a suitable computable approximation (see, e.g., [2, 3, 16, 25]). The overhead of this analysis is the introduction of an auxiliary problem, the so-called adjoint (or dual) problem. The final outcome of the goal-oriented analysis is an a posteriori estimator for the error on the target quantity.

Under reasonable assumptions (see, e.g., [10]) the phenomena at hand can be described by linear advection-diffusion-reaction equations. In particular when considering the transport of a pollutant, strongly advection-dominated flows are routinely involved, which means to deal with situations characterized by evident directional features or steep gradients rather than large curvatures (just think of boundary or internal layers). To sharply capture all these troublesome aspects without spoiling the overall computational cost, an efficient remedy is provided by the widely employed mesh adaption technique. With this respect, a further improvement in terms of saving on the computational cost can be achieved via an anisotropic adaptivity (see, for instance, [5, 15, 17, 27, 1, 8, 12, 19, 32]). The main idea consists of smartly orienting, sizing and shaping the elements of the computational mesh at hand in order to both contain the number of the d.o.f.'s and increase the numerical accuracy.
In this paper we combine the goal-oriented framework with the anisotropic setting. This will allow us to control a quantity of interest on a properly adapted mesh, hopefully with the least number of d.o.f.'s as possible. The resulting computational "machinery" turns out to have the good potentialities for facing the environmental problems of interest in an effective way.
The paper is structured as follows. After presenting the mathematical problem at hand in Section 2, we introduce the anisotropic setting in Section 3. An a posteriori error estimator for the energy norm is derived in Section 4. This analysis has to be meant mainly for familiarizing with the a posteriori framework as well as a hint in view of the goal-oriented setting. Some numerical results related to this first a posteriori error estimator are gathered in Section 5 along with the actual adaptive algorithm. Section 6 deals with the goal-oriented a

posteriori analysis. In particular two alternative anisotropic error estimators are addressed and compared numerically in Section 7. Finally some conclusions are drawn in the last section.

## 2 The problem at hand

In this section we introduce our model problem, i.e., the advection-diffusion-reaction (ADR) equation. In more detail, in view of advection dominated cases, we consider a SUPG type stabilized formulation [4]. The ADR equation reads:

$$\begin{cases} -\nabla \cdot (\mu \nabla u) + \mathbf{b} \cdot \nabla u + \gamma u = f & \text{in } \Omega, \\ u = 0 & \text{on } \Gamma_D, \\ \mu \nabla u \cdot \mathbf{n} = g & \text{on } \Gamma_N, \end{cases} \tag{1}$$

where $\Omega \subset \mathbb{R}^2$ is a polygonal domain with boundary $\partial\Omega$, $\Gamma_D$ and $\Gamma_N$ are suitable measurable nonoverlapping partitions of $\partial\Omega$ with $\Gamma_D \neq \emptyset$ and such that $\partial\Omega = \overline{\Gamma}_D \cup \overline{\Gamma}_N$, and $\mathbf{n}$ is the unit outward normal vector to $\partial\Omega$. Moreover we assume that the source $f \in L^2(\Omega)$, the diffusivity $\mu \in L^\infty(\Omega)$, with $\mu \geq \mu_0 > 0$, the reaction coefficient $\gamma \in L^\infty(\Omega)$, the advective field $\mathbf{b} \in [L^\infty(\Omega)]^2$, with $\nabla \cdot \mathbf{b} \in L^\infty(\Omega)$ and $-\frac{1}{2}\nabla \cdot \mathbf{b} + \gamma \geq 0$, a.e. in $\Omega$, and the Neumann datum $g \in L^2(\Gamma_N)$ are assigned functions.
Notice that throughout the paper, we use a standard notation to denote the Sobolev spaces of functions with Lebesgue measurable derivatives and their norm [20].
The weak form of (1) is:

$$\text{find } u \in V \ : \ B(u, v) = F(v) \quad \forall v \in V, \tag{2}$$

where $V = H^1_{\Gamma_D}(\Omega) = \{v \in H^1(\Omega) : v|_{\Gamma_D} = 0\}$, while the bilinear form $B(\cdot, \cdot)$ and the linear functional $F(\cdot)$ are:

$$B(u, v) = \int_\Omega (\mu \nabla u \cdot \nabla v + \mathbf{b} \cdot \nabla u \ v + \gamma u v) \ d\Omega, \tag{3}$$

$$F(v) = \int_\Omega f v \ d\Omega + \int_{\Gamma_N} g v \ d\Gamma. \tag{4}$$

Existence and uniqueness of the solution of (2) follow immediately from the above hypotheses ([26]).
In order to discretize problem (2), let $\{\mathcal{T}_h\}_h$ be a family of conforming decompositions [6] of $\overline{\Omega}$ into triangles $K$ of diameter $h_K$, such that there is always a vertex of $\mathcal{T}_h$ on the interface between $\Gamma_D$ and $\Gamma_N$. Let $V_h = \{v_h \in C^0(\overline{\Omega}) : v_h|_K \in \mathbb{P}_1, \forall K \in \mathcal{T}_h, \ v_h|_{\Gamma_D} = 0\} \subset V$ denote the subspace of affine functions, $\mathbb{P}_1$ being the space of polynomials of (total) degree less than or equal to one.
As we are interested in applications where advection may strongly dominate over diffusion and reaction, a proper discretization scheme must be employed to limit the spurious oscillations of the numerical solution. Thus we consider the strongly consistent SUPG type method:

$$\text{find } u_h \in V_h \ : \ B_h(u_h, v_h) = F_h(v_h) \quad \forall v_h \in V_h, \tag{5}$$

with

$$B_h(u,v) = B(u,v) + \sum_{K\in\mathcal{T}_h} \tau_K \left(-\nabla\cdot(\mu\nabla u) + \mathbf{b}\cdot\nabla u + \gamma u, \mathbf{b}\cdot\nabla v\right)_K, \qquad (6)$$

$$F_h(v) = F(v) + \sum_{K\in\mathcal{T}_h} \tau_K \left(f, \mathbf{b}\cdot\nabla v\right)_K, \qquad (7)$$

where $(\cdot,\cdot)_K$ denotes the $L^2$-inner product on $K$, while $\tau_K$ are suitable stabilization parameters to be defined later (see Remark 3.3).
By simply subtracting (5) from (2), with $v = v_h$, we get the "skew orthogonality" property

$$B(e_h, v_h) = \sum_{K\in\mathcal{T}_h} \tau_K \left(-\nabla\cdot(\mu\nabla u_h) + \mathbf{b}\cdot\nabla u_h + \gamma u_h - f, \mathbf{b}\cdot\nabla v_h\right)_K \quad \forall v_h \in V_h, \qquad (8)$$

$e_h = u - u_h$ being the discretization error. If further $u$ enjoys a higher regularity, i.e. $u \in \{v \in H^1(\Omega) : \nabla\cdot(\mu\nabla v) \in L^2(K), \forall K \in \mathcal{T}_h\}$, the standard Galerkin orthogonality property with respect to the stabilized bilinear form $B_h(\cdot,\cdot)$ holds

$$B_h(e_h, v_h) = 0 \quad \forall v_h \in V_h. \qquad (9)$$

## 3 The anisotropic framework

Throughout this section we recall the anisotropic framework ([11, 12, 13]) on which the a posteriori analysis is based.

Let us consider the standard invertible affine map $T_K : \widehat{K} \to K$ from a reference triangle $\widehat{K}$ to the general one $K \in \mathcal{T}_h$, such that, for any $\mathbf{x} \in K$

$$\mathbf{x} = (x_1, x_2)^T = T_K(\widehat{\mathbf{x}}) = M_K\widehat{\mathbf{x}} + \mathbf{t}_K \quad \text{with} \quad \widehat{\mathbf{x}} \in \widehat{K}, \qquad (10)$$

where $M_K \in \mathbb{R}^{2\times 2}$ and $\mathbf{t}_K \in \mathbb{R}^2$. The most suitable choice for $\widehat{K}$ coincides with the triangle with vertices $(-\sqrt{3}/2, -1/2)$, $(\sqrt{3}/2, -1/2)$, $(0, 1)$, that is with the equilateral triangle inscribed in the unit circle, with barycenter located at the origin.
The anisotropic information of each triangle $K$ is derived moving from the spectral properties of the Jacobian $M_K$. First let us introduce the polar decomposition $M_K = B_K Z_K$ of $M_K$ into a symmetric positive definite and an orthogonal matrix, $B_K$, $Z_K \in \mathbb{R}^{2\times 2}$, respectively. Then let us further factorize the matrix $B_K$ in terms of its eigenvectors $\mathbf{r}_{i,K}$ and eigenvalues $\lambda_{i,K}$, with $i = 1, 2$, as $B_K = R_K^T \Lambda_K R_K$ with $\Lambda_K = \mathrm{diag}(\lambda_{1,K}, \lambda_{2,K})$ and $R_K^T = [\mathbf{r}_{1,K}, \mathbf{r}_{2,K}]$. Thus the shape and the orientation of each element $K$ are completely characterized by these quantities: the eigenvectors $\mathbf{r}_{i,K}$ provide us with the directions of the semi-axes of the ellipse circumscribing $K$, while the eigenvalues $\lambda_{i,K}$ measure the length of such semi-axes (see Fig. 1).

**Remark 3.1** *In the analysis below $Z_K$ and $\mathbf{t}_K$ do not play any role as they are associated with a rigid rotation and a shift, respectively.*

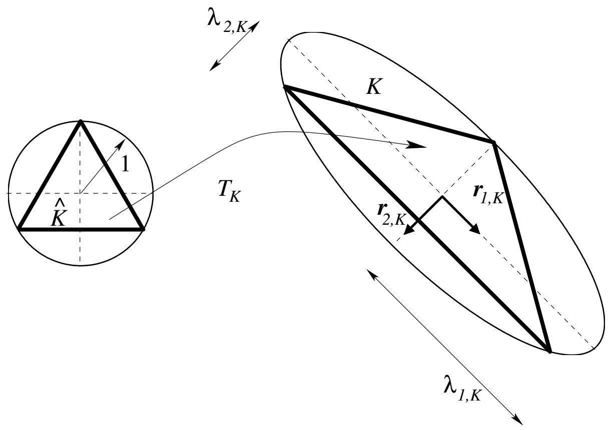


Figure 1: The affine map $T_K$ from the reference triangle $\widehat{K}$ to the triangle $K$ with the geometrical quantities $\lambda_{1,K}$, $\lambda_{2,K}$, $\mathbf{r}_{1,K}$ and $\mathbf{r}_{2,K}$ highlighted.

Without loosing generality, we assume that $\lambda_{1,K} \geq \lambda_{2,K}$, so that the so-called stretching factor is

$$s_K = \frac{\lambda_{1,K}}{\lambda_{2,K}} \geq 1, \tag{11}$$

$s_{\widehat{K}}$ being identically equal to 1.

In view of the a posteriori analysis in Sections 4 and 6, we introduce the Clément interpolant ([7]), defined, in the case of linear finite elements, as

$$I_h^1 v(\mathbf{x}) = \sum_{N_j \in N_\Omega \cup N_{\Gamma_N}} P_j v(N_j) \varphi_j(\mathbf{x}) \quad \forall v \in L^2(\Omega), \tag{12}$$

where $\varphi_j$ is the Lagrangian basis function associated with the node $N_j$, while $P_j v$ denotes the plane associated with the patch $\Delta_j$ of the elements sharing node $N_j$ and defined by the relations

$$\int_{\Delta_j} (P_j v - v)\psi \; d\Omega = 0 \quad \text{with } \psi = 1, x_1, x_2. \tag{13}$$

Notice that the sum in (12) runs only on the internal mesh vertices $N_\Omega$ and on those on the Neumann boundary $N_{\Gamma_N}$.
Due to the local feature of the anisotropic interpolation estimates, we refer to the restriction of $I_h^1 v$ to the element $K$ as $I_K^1 v$.
Under the further assumptions

$$\#\Delta_K \leq N \quad \text{and} \quad \operatorname{diam}(T_K^{-1}(\Delta_K)) \leq C_\Delta \simeq O(1), \tag{14}$$

with card $\cdot$ and diam$(\cdot)$ the cardinality and the diameter of a given set, the constant $C_\Delta \geq h_{\widehat{K}}$, and $\Delta_K$ denoting the patch of all the elements sharing at least a vertex with $K$, we can prove (see [12, 13, 23]) the following

**Proposition 3.1** *Let $v \in H^1(\Omega)$. Then there exist constants $C_i = C_i(N, C_\Delta)$, with $i = 1, 2, 3$, such that, for any $K \in \mathcal{T}_h$, it holds*

$$\|v - I_K^1 v\|_{L^2(K)} \leq C_1 \left[ \sum_{i=1}^{2} \lambda_{i,K}^2 \left( \mathbf{r}_{i,K}^T G_K(v) \mathbf{r}_{i,K} \right) \right]^{1/2}, \tag{15}$$

$$|v - I_K^1 v|_{H^1(K)} \leq C_2 \frac{1}{\lambda_{2,K}} \left[ \sum_{i=1}^{2} \lambda_{i,K}^2 \left( \mathbf{r}_{i,K}^T G_K(v) \mathbf{r}_{i,K} \right) \right]^{1/2}, \tag{16}$$

$$\|v - I_K^1 v\|_{L^2(\partial K)} \leq C_3 h_K^{\frac{1}{2}} \left[ s_K \left( \mathbf{r}_{1,K}^T G_K(v) \mathbf{r}_{1,K} \right) + \frac{1}{s_K} \left( \mathbf{r}_{2,K}^T G_K(v) \mathbf{r}_{2,K} \right) \right]^{1/2}, \tag{17}$$

*where*

$$G_K(v) = \sum_{T \in \Delta_K} \begin{bmatrix} \displaystyle\int_T \left( \frac{\partial v}{\partial x} \right)^2 d\Omega & \displaystyle\int_T \left( \frac{\partial v}{\partial x} \right) \left( \frac{\partial v}{\partial y} \right) d\Omega \\ \displaystyle\int_T \left( \frac{\partial v}{\partial x} \right) \left( \frac{\partial v}{\partial y} \right) d\Omega & \displaystyle\int_T \left( \frac{\partial v}{\partial y} \right)^2 d\Omega \end{bmatrix} \tag{18}$$

*is a $2 \times 2$ symmetric positive semi-definite matrix.*

**Remark 3.2** *Conditions* (14) *essentially avoid too distorted patches in the reference framework. This eases the derivation of the interpolation estimates above as they are actually carried out in the reference setting and then mapped back to the general one. On the other hand, the same conditions do not limit the anisotropic features (stretching factor and orientation) of each $K$ in $\Delta_K$, but rather the corresponding variation in $\Delta_K$ (see* [24] *for examples of acceptable and not acceptable patches).*

Moreover the following result holds (see [23] for the proof):

**Proposition 3.2** *For any function $v \in H^1(\Omega)$ and two constants $\alpha, \beta > 0$, it holds*

$$\min\{\alpha, \beta\} \leq \frac{\alpha \left( \mathbf{r}_{1,K}^T G_K(v) \mathbf{r}_{1,K} \right) + \beta \left( \mathbf{r}_{2,K}^T G_K(v) \mathbf{r}_{2,K} \right)}{|v|_{H^1(\Delta_K)}^2} \leq \max\{\alpha, \beta\}, \tag{19}$$

*$G_K(\cdot)$ being defined as in* (18).

**Remark 3.3** *With reference to the SUPG type stabilized formulation* (5)-(7), *the following anisotropic recipe is used:*

$$\tau_K = \begin{cases} \dfrac{\lambda_{2,K}^2}{12\mu_K} & \text{if } \mathbb{P}e_K < 1, \\ \dfrac{\lambda_{2,K}}{2\|\mathbf{b}\|_{L^\infty(K)}} & \text{if } \mathbb{P}e_K \geq 1, \end{cases} \tag{20}$$

*where $\mathbb{P}e_K = \lambda_{2,K} \|\mathbf{b}\|_{L^\infty(K)} / (6\mu_K)$ is the local Péclet number, while $\mu_K = \min_{\mathbf{x} \in K} \mu(\mathbf{x})$* [24].

# 4 An a posteriori error estimator for the energy norm

In this section we derive an anisotropic a posteriori error estimate for the energy norm $|||e_h||| = (B(e_h, e_h))^{1/2}$ of the discretization error associated with the ADR equation (1). In more detail we move from a standard residual-based approach [33] properly combined with the anisotropic analysis in Section 3. The present analysis generalizes the result in [28] to the case of a non-constant convective term as well as to mixed boundary conditions.

First let us anticipate some notations used in the main result of this section. For any $K \in \mathcal{T}_h$, let

$$r_K(u_h) = \left(f + \nabla \cdot (\mu \nabla u_h) - \mathbf{b} \cdot \nabla u_h - \gamma u_h\right)|_K, \tag{21}$$

and

$$j_K(u_h)|_E = \begin{cases} 0 & \text{for any } E \in \partial K \cap \mathcal{E}_{h,D}, \\ 2\left(g - (\mu \nabla u_h)|_K \cdot \mathbf{n}_K\right)|_E & \text{for any } E \in \partial K \cap \mathcal{E}_{h,N}, \\ -\left[\mu \nabla u_h \cdot \mathbf{n}\right]_E & \text{for any } E \in \partial K \cap \mathcal{E}_{h,int}, \end{cases} \tag{22}$$

be the interior and the boundary residuals associated with the approximation $u_h$, respectively, where $\mathcal{E}_{h,int}$ denotes the set of the internal edges of the skeleton $\mathcal{E}_h$ of the triangulation $\mathcal{T}_h$, while $\mathcal{E}_{h,D}$ and $\mathcal{E}_{h,N}$ stand for the Dirichlet and Neumann subset of $\mathcal{E}_h$, respectively. With the notation

$$\left[\mu \nabla u_h \cdot \mathbf{n}\right]_E := (\mu \nabla u_h)|_K \cdot \mathbf{n}_K + (\mu \nabla u_h)|_{K'} \cdot \mathbf{n}_{K'} \tag{23}$$

defined on the edge $E$ separating elements $K$ and $K'$, we refer to the jump of the diffusive flux on the interface.

We are in a position to state the desired anisotropic error estimate (see also [23, 28]).

**Proposition 4.1** *Let $u \in V$ be the solution of the weak problem* (2) *and $u_h \in V_h$ be the corresponding approximation via* (5). *Then it holds*

$$|||e_h||| \leq C \left( \sum_{K \in \mathcal{T}_h} \alpha_K \rho_K(u_h) w_K(e_h) \right)^{1/2}, \tag{24}$$

*with $\alpha_K = (\lambda_{1,K}\lambda_{2,K})^{1/2}$,*

$$\rho_K(u_h) = \left(1 + \tau_K \frac{\|\mathbf{b}\|_{L^\infty(K)}}{\lambda_{2,K}}\right) \|r_K(u_h)\|_{L^2(K)} + \frac{1}{2}\left(\frac{h_K}{\lambda_{1,K}\lambda_{2,K}}\right)^{1/2} \|j_K(u_h)\|_{L^2(\partial K)}, \tag{25}$$

$$w_K(e_h) = \left[ s_K \left(\mathbf{r}_{1,K}^T G_K(e_h) \mathbf{r}_{1,K}\right) + \frac{1}{s_K}\left(\mathbf{r}_{2,K}^T G_K(e_h) \mathbf{r}_{2,K}\right)\right]^{1/2}, \tag{26}$$

*where $C = C(N, C_\Delta)$, $\tau_K$ is the stabilization parameter defined as in* (20), *the matrix $G_K(\cdot)$ is defined as in* (18), *while the residuals $r_K(u_h)$ and $j_K(u_h)$ are given by* (21) *and* (22), *respectively.*

**Proof.** From the definition (3) of the bilinear form $B(\cdot,\cdot)$ and thanks to the weak form (2), we have

$$\begin{aligned} B(e_h,v) &= F(v) - B(u_h,v) = \sum_{K\in\mathcal{T}_h}\left\{\int_K fv\ d\Omega + \int_{\partial K\cap\Gamma_N} gv\ d\Gamma\right\} \\ &- \sum_{K\in\mathcal{T}_h}\int_K (\mu\nabla u_h\cdot\nabla v + \mathbf{b}\cdot\nabla u_h\ v + \gamma u_h v)\ d\Omega, \end{aligned} \tag{27}$$

for any $v \in V$. Notice that we have split the integrals element-wise with the aim of localizing the a posteriori estimator. After integrating by parts in the second sum at the right-hand side of (27), we obtain

$$\begin{aligned} B(e_h,v) &= \sum_{K\in\mathcal{T}_h}\left\{\int_K fv\ d\Omega + \int_{\partial K\cap\Gamma_N} gv\ d\Gamma\right\} \\ &- \sum_{K\in\mathcal{T}_h}\left\{\int_K (-\nabla\cdot(\mu\nabla u_h) + \mathbf{b}\cdot\nabla u_h + \gamma u_h)\, v\ d\Omega\right. \\ &+ \left.\int_{\partial K\cap\mathcal{E}_{h,N}} \mu\nabla u_h\cdot\mathbf{n}_K v\ d\Gamma + \int_{\partial K\cap\mathcal{E}_{h,int}} \mu\nabla u_h\cdot\mathbf{n}_K v\ d\Gamma\right\}. \end{aligned} \tag{28}$$

Observe that the integration by parts is possible consistently with the regularity of $u_h$ since we are working on each element $K$. Thanks to the definitions (21) and (22), we get

$$B(e_h,v) = \sum_{K\in\mathcal{T}_h}\left\{\int_K r_K(u_h)v\ d\Omega + \frac{1}{2}\int_{\partial K} j_K(u_h)v\ d\Gamma\right\}, \tag{29}$$

the factor $1/2$ taking into account the fact that each internal edge $E$ shares two elements of the triangulation. A suitable combination of the "skew orthogonality" property (8) together with the definition (21) of the internal residual $r_K(u_h)$ and with identity (29) (also used with $v = v_h$), yields

$$\begin{aligned} B(e_h,v) &= B(e_h,v) - B(e_h,v_h) - \sum_{K\in\mathcal{T}_h}\tau_K\,(r_K(u_h),\mathbf{b}\cdot\nabla v_h)_{L^2(K)} \\ &= \sum_{K\in\mathcal{T}_h}\left\{\int_K r_K(u_h)(v-v_h)\ d\Omega + \frac{1}{2}\int_{\partial K} j_K(u_h)(v-v_h)\ d\Gamma\right. \\ &- \left.\tau_K\int_K r_K(u_h)\mathbf{b}\cdot\nabla v_h\ d\Omega\right\}. \end{aligned} \tag{30}$$

Adding and subtracting the quantity $\tau_K\displaystyle\int_K r_K(u_h)\mathbf{b}\cdot\nabla v\ d\Omega$ to (30) and using the Cauchy-Schwarz inequality, we have

$$\begin{aligned} |B(e_h,v)| &\le \sum_{K\in\mathcal{T}_h}\Big\{\|r_K(u_h)\|_{L^2(K)}\big[\|v-v_h\|_{L^2(K)} \\ &+ \tau_K\,\|\mathbf{b}\cdot\nabla(v-v_h)\|_{L^2(K)} + \tau_K\,\|\mathbf{b}\cdot\nabla v\|_{L^2(K)}\big] \\ &+ \frac{1}{2}\|j_K(u_h)\|_{L^2(\partial K)}\|v-v_h\|_{L^2(\partial K)}\Big\}. \end{aligned} \tag{31}$$

The two terms involving the advective field $\mathbf{b}$ can be further bounded as

$$\begin{aligned} \|\mathbf{b}\cdot\nabla(v-v_h)\|_{L^2(K)} &\le \|\mathbf{b}\|_{L^\infty(K)}\ |v-v_h|_{H^1(K)}, \\ \|\mathbf{b}\cdot\nabla v\|_{L^2(K)} &\le \|\mathbf{b}\|_{L^\infty(K)}\ |v|_{H^1(K)}, \end{aligned} \tag{32}$$

while, from Proposition 3.2 with $\alpha = s_K$ and $\beta = 1/s_K$, it holds

$$|v|_{H^1(K)} \leq |v|_{H^1(\Delta_K)} \leq \frac{1}{\lambda_{2,K}} \left[ \sum_{i=1}^{2} \lambda_{i,K}^2 \left( \mathbf{r}_{i,K}^T G_K(v) \mathbf{r}_{i,K} \right) \right]^{1/2}. \tag{33}$$

Coming back to (31) and choosing the arbitrary function $v_h$ as the Clément interpolant of $v$, i.e. $v_h = I_h^1 v \in V_h$, we can exploit Proposition 3.1 along with relations (32) and (33) to get

$$\begin{aligned} |B(e_h, v)| \leq \sum_{K \in \mathcal{T}_h} \Bigg\{ \Big[ (\lambda_{1,K}\lambda_{2,K})^{1/2} \left( C_1 + (1 + C_2)\, \tau_K \frac{\|\mathbf{b}\|_{L^\infty(K)}}{\lambda_{2,K}} \right) \|r_K(u_h)\|_{L^2(K)} \\ + C_3 \frac{1}{2} h_K^{1/2} \|j_K(u_h)\|_{L^2(\partial K)} \Big] \Big[ s_K \left( \mathbf{r}_{1,K}^T G_K(v) \mathbf{r}_{1,K} \right) + \frac{1}{s_K} \left( \mathbf{r}_{2,K}^T G_K(v) \mathbf{r}_{2,K} \right) \Big]^{1/2} \Bigg\}. \end{aligned} \tag{34}$$

Result (24) follows after taking $v = e_h$ and identifying $C$ with $\max\{C_1, 1 + C_2, C_3\}$. $\diamond\square$

Notice that estimate (24) is not useful yet in view, for instance, of an adaptive procedure, the right-hand side depending on the discretization error $e_h$ itself. On the other hand, due to the presence of such error, we expect the whole right-hand side of (24) to go to zero, as the mesh gets finer and finer. In order to exploit this nice feature we aim at approximating the weights $w_K(e_h)$ in (24) via suitable computable quantities. Due to their dependence on the first-order derivatives of the error, a convenient strategy consists of resorting to the well-known Zienkiewicz-Zhu (ZZ) recovery procedure [34, 35, 36]. Denoting the recovered gradient of $u_h$ with $\nabla^{ZZ} u_h = \left( (\nabla^{ZZ} u_h)_1, (\nabla^{ZZ} u_h)_2 \right)^T$, we substitute the matrix $G_K(e_h)$ in the definition (26) of $w_K(e_h)$ with

$$[G_K(e_h^*)]_{i,j} = \sum_{T \in \Delta_K} \int_T \left( (\nabla^{ZZ} u_h)_i - \frac{\partial u_h}{\partial x_i} \right) \left( (\nabla^{ZZ} u_h)_j - \frac{\partial u_h}{\partial x_j} \right) d\Omega, \tag{35}$$

for $i, j = 1, 2$. We can now define the fully computable a posteriori error estimator which will drive the anisotropic mesh adaption procedure used throughout the numerical validation in the section below.

**Definition 4.1** *Let $u_h \in V_h$ be the solution of the discrete problem* (5)*. Then the energy norm of the discretization error $e_h$ can be estimated by the quantity*

$$\eta = \left( \sum_{K \in \mathcal{T}_h} \eta_K^2 \right)^{1/2}, \tag{36}$$

*the local indicator $\eta_K$ being given by*

$$\eta_K = \left( \alpha_K \rho_K(u_h) w_K(e_h^*) \right)^{1/2}, \tag{37}$$

*where $\alpha_K$ and $\rho_K(u_h)$ are defined as in Proposition 4.1, while*

$$w_K(e_h^*) = \left[ s_K \left( \mathbf{r}_{1,K}^T G_K(e_h^*) \mathbf{r}_{1,K} \right) + \frac{1}{s_K} \left( \mathbf{r}_{2,K}^T G_K(e_h^*) \mathbf{r}_{2,K} \right) \right]^{1/2}. \tag{38}$$

**Remark 4.1** *The isotropic counterpart of the estimator* (36) *can be obtained by enforcing* $\lambda_{1,K} = \lambda_{2,K} \simeq h_K$. *Notice that with this choice the weight* (26) *collapses to* $|e_h|_{H^1(\Delta_K)}$. *No gradient recovery procedure is needed, a simplification of such a term occurring in this case (see the derivation of standard residual based error estimators, for instance in* [33]*).*

**Remark 4.2** *The general structure of the recovered gradient* $\nabla^{ZZ} u_h$ *is*

$$\nabla^{ZZ} u_h(\mathbf{x}) = \sum_{N_j \in N_{\overline{\Omega}}} \nabla^{ZZ} u_h(N_j) \varphi_j(\mathbf{x}), \tag{39}$$

$N_{\overline{\Omega}}$ *being the set of all the nodes in* $\mathcal{T}_h$. *Observe that* $\nabla^{ZZ} u_h$ *is piecewise linear, the hat functions* $\varphi_j$ *coinciding with the hat basis functions of* $V_h$. *Different recipes are available in the literature to compute the coefficients* $\nabla^{ZZ} u_h(N_j)$ *(see, for instance,* [21, 30, 34, 35, 36]*). One of the most popular choice, namely the continuous SPR procedure, can be related to the previously defined Clément interpolant* $I_h^1$. *In more detail, it suffices picking* $v = \partial u_h / \partial x_i$, *for* $i = 1, 2$, *in* (12) *and* (13). *If further one approximates the mass matrix involved in* (13) *via the trapezoidal quadrature rule, then one obtains for the coefficients in* (39) *the explicit expression*

$$\nabla^{ZZ} u_h(N_j) = \frac{1}{|\Delta_j|} \sum_{T \in \Delta_j} |T| \, (\nabla u_h)|_T, \tag{40}$$

$|\cdot|$ *denoting the d-measure function, with* $d = 1, 2$ *(see* [30]*). Recipe* (39)-(40) *will be employed in all the numerical test cases.*

# 5 Control of the energy norm: numerical assessment

The purpose of this section is twofold: first we provide an actual procedure to exploit the a posteriori error estimator (36), then some numerical results are discussed.

## 5.1 The adaptive procedure

We employ a metric-based adaptive procedure exploiting the estimator (36) in a predictive fashion. Two different approaches are typically pursued:

(a) given a constraint on the maximum number of elements, find the mesh providing the most accurate numerical solution;

(b) given a constraint on the accuracy of the numerical solution, find the mesh with the least number of elements.

We here detail the (b) approach, while providing some comments on the (a) one in Remark 5.1. Let us first recall that a metric is induced by a symmetric positive definite tensor field $\widetilde{M} : \Omega \longrightarrow \mathbb{R}^2$. We aim at clarifying the interplay between metric and mesh. For any given mesh $\mathcal{T}_h$, we can define a piecewise constant metric $\widetilde{M}_{\mathcal{T}_h}$, such that, $\widetilde{M}_{\mathcal{T}_h}|_K = \widetilde{M}_K = B_K^{-2} = R_K^T \Lambda_K^{-2} R_K$, for any

$K \in \mathcal{T}_h$, the matrices being the ones defined in Section 3. With respect to this metric, any triangle $K$ is unit equilateral, i.e.

$$\|e\|_{\widetilde{M}_{\mathcal{T}_h}} = \int_0^{|e|} \sqrt{\mathbf{t}^T \widetilde{M}_{\mathcal{T}_h}(s)\mathbf{t}}\ ds = 1,$$

with $\mathbf{t}$ the unit tangent vector along the edge $e$.
Suppose now that a metric $\widetilde{M}$ is given. We show how an optimal mesh with respect to $\widetilde{M}$ can be defined in terms of a "matching condition". With this respect, it is convenient to diagonalize the tensor field $\widetilde{M}$ as $\widetilde{M} = \widetilde{R}^T \widetilde{\Lambda}^{-2} \widetilde{R}$, with $\widetilde{\Lambda} = \mathrm{diag}(\widetilde{\lambda}_1, \widetilde{\lambda}_2)$ and $\widetilde{R}^T = [\widetilde{\mathbf{r}}_1, \widetilde{\mathbf{r}}_2]$ positive diagonal and orthogonal matrices, respectively. For practical reasons, we approximate the quantities $\widetilde{\lambda}_1$, $\widetilde{\lambda}_2$, $\widetilde{\mathbf{r}}_1$ and $\widetilde{\mathbf{r}}_2$ defining $\widetilde{M}$ by piecewise constant functions over the triangulation $\mathcal{T}_h$, such that $\widetilde{\mathbf{r}}_i|_K = \widetilde{\mathbf{r}}_{i,K}$, $\widetilde{\lambda}_i|_K = \widetilde{\lambda}_{i,K}$, for any $K \in \mathcal{T}_h$ and with $i = 1, 2$. Then we introduce the *matching condition*:

**Definition 5.1** *A mesh $\mathcal{T}_h$ matches a given metric $\widetilde{M}$ if, for any $K \in \mathcal{T}_h$,*

$$\widetilde{M}|_K = \widetilde{M}_{\mathcal{T}_h}|_K, \tag{41}$$

*i.e. $\widetilde{\mathbf{r}}_{i,K} = \mathbf{r}_{i,K}$, $\widetilde{\lambda}_{i,K} = \lambda_{i,K}$, for $i = 1, 2$.*

We stress that in our case the tensor field $\widetilde{M}$ is not explicitly given. Rather it must be obtained by solving the optimization problem (b) reformulated with respect to the optimal metric (rather than the optimal mesh) in view of Definition 5.1. Thus the optimal metric will be our actual "unknown".
In more detail, the determination of $\widetilde{M}$ and of the corresponding matching triangulation is obtained via an iterative method. For clarity, we point out that, at each iteration $j$, we deal with three entities: the actual mesh $\mathcal{T}_h^{(j)}$, the new metric $\widetilde{M}^{(j+1)}$ computed on $\mathcal{T}_h^{(j)}$, and the updated mesh $\mathcal{T}_h^{(j+1)}$ matching $\widetilde{M}^{(j+1)}$. Problem (5) is first solved on $\mathcal{T}_h^{(j)}$. Then its solution is used to set up suitable local optimization problems, with the aim of identifying the metric $\widetilde{M}^{(j+1)}$ approximating the optimal metric $\widetilde{M}$, solution to (b). Via the matching condition (41), the new mesh $\mathcal{T}_h^{(j+1)}$ is then built. Let us detail the local optimization procedure. We rewrite the local estimator $\eta_K$ in (37) as

$$\eta_K^2 = \frac{|K|^{3/2}}{|\widehat{K}|^{1/2}}\, \widetilde{\rho}_K(u_h) \underbrace{\left[ s_K \left( \mathbf{r}_{1,K}^T \widetilde{G}_K(e_h^*) \mathbf{r}_{1,K} \right) + \frac{1}{s_K} \left( \mathbf{r}_{2,K}^T \widetilde{G}_K(e_h^*) \mathbf{r}_{2,K} \right) \right]^{1/2}}_{(*)}, \tag{42}$$

where

$$\widetilde{\rho}_K(u_h) = \frac{\rho_K(u_h)}{|K|^{1/2}} \quad \text{and} \quad \widetilde{G}_K(e_h^*) = \frac{G_K(e_h^*)}{|K|} \tag{43}$$

are the scaled residual and recovered gradient matrix, respectively, and the relation $\alpha_K = \sqrt{|K|/|\widehat{K}|}$ has been advocated. This scaling is driven with the aim of making all terms in the right-hand side of (42) approximately independent of the measure of triangle $K$, at least asymptotically (i.e., when the mesh is sufficiently fine), thus lumping this information only in a multiplicative constant. In view of (b) we first observe that minimizing the number of elements is equivalent to maximizing the area $|K|$ of each element. As we demand also that the local error indicator $\eta_K$ be equal to a desired constant (the local tolerance $\tau$) according to an equidistribution criterion, the only way to satisfy (b) is to minimize the term $(*)$ in (42). This amounts to solving the following local constrained minimization problem:

$$\text{find } s_K,\ \mathbf{r}_{1,K} \quad \text{such that}$$

$$I(s_K, \mathbf{r}_{1,K}) = s_K \left( \mathbf{r}_{1,K}^T \widetilde{G}_K(e_h^*) \mathbf{r}_{1,K} \right) + \frac{1}{s_K} \left( \mathbf{r}_{2,K}^T \widetilde{G}_K(e_h^*) \mathbf{r}_{2,K} \right) \quad \text{is minimum,} \tag{44}$$

with $s_K \geq 1$, $\|\mathbf{r}_{1,K}\|_2 = \|\mathbf{r}_{2,K}\|_2 = 1$ and $\mathbf{r}_{1,K} \cdot \mathbf{r}_{2,K} = 0$, $\|\cdot\|_2$ denoting the standard Euclidean norm. The solution to this problem is given in the following

**Proposition 5.1** *The solution* $(\widetilde{s}_K, \widetilde{\mathbf{r}}_{1,K})$ *of* (44) *is given by*

$$\widetilde{s}_K = \sqrt{\frac{\sigma_{1,K}}{\sigma_{2,K}}}, \qquad \widetilde{\mathbf{r}}_{1,K} = \mathbf{p}_{2,K}, \tag{45}$$

$\sigma_{1,K}$ *and* $\sigma_{2,K}$ *being the maximum and minimum eigenvalues of the matrix* $G_K(e_h^*)$*, while* $\mathbf{p}_{1,K}$ *and* $\mathbf{p}_{2,K}$ *are the associated eigenvectors.*

For the corresponding proof see [23] where we provide also a practical recipe to by-pass the rare occurrence $\sigma_{2,K} = 0$. In order to fully compute $\widetilde{M}^{(j+1)}$, after computing $\widetilde{s}_K$ and $\widetilde{\mathbf{r}}_{1,K}$, we need only to compute the two eigenvalues $\widetilde{\lambda}_{1,K}$ and $\widetilde{\lambda}_{2,K}$ separately. This is achieved by resorting to the above-cited equidistribution principle ($\eta_K = \tau$, $\forall K$), yielding

$$\widetilde{\lambda}_{1,K} = \sqrt{\widetilde{s}_K q}, \qquad \widetilde{\lambda}_{2,K} = \sqrt{\frac{q}{\widetilde{s}_K}}, \tag{46}$$

with

$$q = \left[ \frac{\tau^4}{|\widehat{K}|^2 (\widetilde{\rho}_K(u_h))^2 \left( \widetilde{s}_K \sigma_{2,K} + \sigma_{1,K}/\widetilde{s}_K \right)} \right]^{1/3}. \tag{47}$$

To summarize, the adaptive algorithm used in practice reads

1. `set` $j = 0$ `and build the background mesh` $\mathcal{T}_h^{(j)}$`;`
2. `solve problem (5);`
3. `solve the local minimization problem (44) for` $\widetilde{s}_K$ `and` $\widetilde{\mathbf{r}}_{1,K}$`;`
4. `via the equidistribution principle, compute` $\widetilde{\lambda}_{1,K}$ `and` $\widetilde{\lambda}_{2,K}$`;`
5. `build up the new metric` $\widetilde{M}^{(j+1)}$`;`
6. `construct the new mesh` $\mathcal{T}_h^{(j+1)}$ `matching the metric` $\widetilde{M}^{(j+1)}$`;`
7. `if a suitable stopping criterion is met, exit; else go to (2).`

**Remark 5.1** *If one is interested in the approach* (a), *the above adaptive procedure can be recycled except for the choice of the tolerance $\tau$ which is not any more user-defined, but it depends on the desired number of elements.*

## 5.2 Numerical tests

Now we shall assess the reliability of the anisotropic a posteriori error estimator (36). In particular we compare the performance of such estimator with the isotropic corresponding one (see Remark 4.1), still driven by a metric based approach. The mesh generator employed in all test cases below is BAMG [18].

*Test case $E1$: the "ramp" case.*
This is an academic test case with available exact solution aiming at providing a quantitative analysis of the proposed estimator. In more detail, referring to the ADR equation (1), we assume $\mu = 10^{-3}$, $\mathbf{b} = (1,0)^T$, $\gamma = 0$, $\Omega = (0,4) \times (-1,1)$, $\Gamma_D = \partial\Omega$, and the source term $f$ is chosen such that the exact solution of (1) is

$$u(x_1, x_2) = x_1 \left(1 - e^{-50(4-x_1)}\right) \left(1 - e^{-50(x_2+1)} - e^{-50(1-x_2)}\right), \qquad (48)$$

exhibiting three boundary layers along the horizontal and outflow boundaries (see Fig. 2). Notice that we are in the presence of a highly advection dominated problem as the global Peclét number is $\mathbb{P}e = \|\mathbf{b}\|_{L^\infty(\Omega)} L/(2\mu) = 2000$, with $L = 4$.

In the spirit of approaches (a) and (b) of the above adaptive procedure, we carry out two comparisons, with the same accuracy and with the same number of elements. In Fig. 4 we compare the meshes obtained employing the anisotropic (left) and isotropic (right) estimator with a similar accuracy on the exact error equal to 0.33. Notice that in the anisotropic case only 500 elements are required versus 3200 demanded in the isotropic case. Moreover most of the triangles in the anisotropic case are stretched along the three boundary layers.
Figure 3 shows the meshes (anisotropic on the left and isotropic on the right)

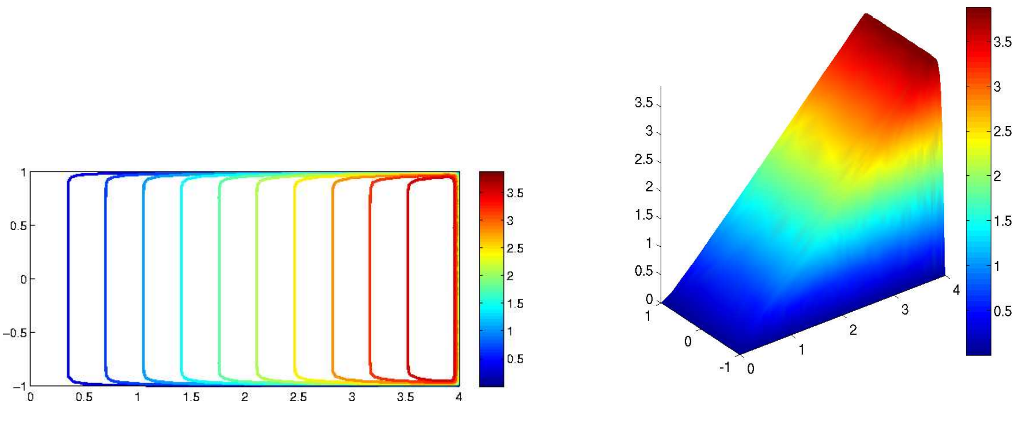

Figure 2: Contour-lines (left) and surface plot (right) of the exact solution for test case $E1$.

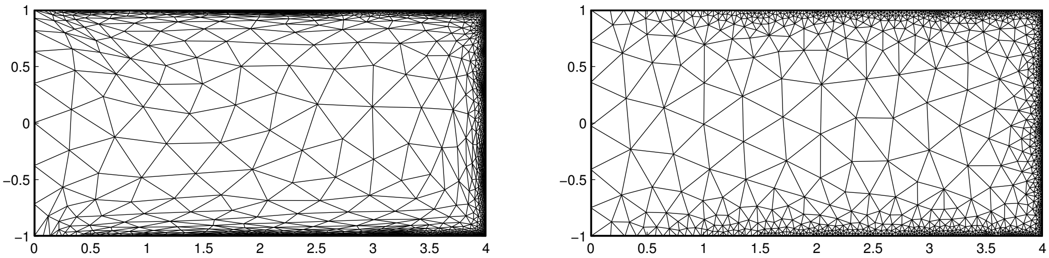

Figure 3: Anisotropic (left) versus isotropic (right) adapted mesh with the same number of elements (2500) for test case $E1$.

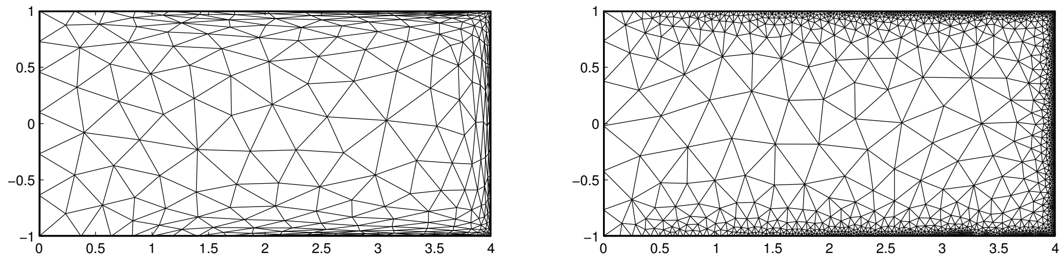

Figure 4: Anisotropic (left) versus isotropic (right) adapted mesh with a similar accuracy (0.33) for test case $E1$.

obtained by fixing the number of mesh elements chosen equal to 2500. The energy norm of the error in the anisotropic case is $1.38 \cdot 10^{-1}$ compared with the value $3.92 \cdot 10^{-1}$ for the isotropic case, yielding a gain of 1/3 in accuracy. Observe that the additional 2000 triangles of the anisotropic grid with respect to Fig. 4 are essentially "squeezed" in the boundary layers, the central area remaining almost unchanged. In Fig. 5 we highlight a detail of the meshes in Fig. 4 (on the left) and Fig. 3 (on the right) in correspondence with a portion of the outflow boundary. In both cases the anisotropic grids are clearly stretched along the boundary layer, thus allowing for a sharper capturing of the steep solution. Analogous comments hold for the horizontal boundary layers except that, as these are parabolic layers, their thickness is $O(\sqrt{\mu})$ while the outflow boundary is $O(\mu)$ large.

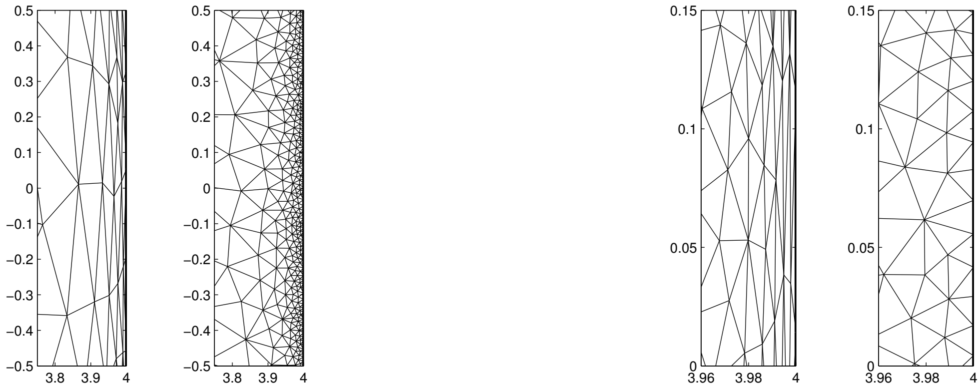


Figure 5: Zooms of the adapted meshes in Fig. 4 (left) and 3 (right) for test case $E1$.

Now we check the convergence properties of the proposed adaptive procedure.

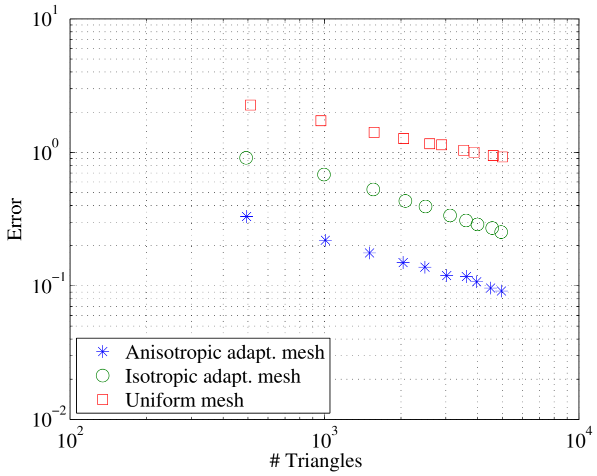


Figure 6: Convergence histories associated with the uniform refinement ($\square$), anisotropic adapted mesh ($*$) and the isotropic one (O) for test case $E1$.

In particular, in Fig. 6 we compare the convergence histories characterizing both the anisotropic and isotropic error estimators along with that associated with a uniform refinement. The trend for the first two estimators exhibits the same slope even if the line corresponding to the anisotropic estimator is shifted below the isotropic one. The mesh adaption driven by uniform refinement seems to lead to a slower convergence. The conclusions drawn from Figs 4 and 3 are further justified by Fig. 6: the error reduction is about 1/3 for the anisotropic versus the isotropic case with the same number of elements, while the saving in the number of elements is about 6-7 times as much.

In Table 1 we deal with the computational cost issue[1]. From the first row

[1]The computations are carried out on an AMD Athlon 1.33 GHz processor, with 256 KB of

Table 1: CPU time (in seconds) for the anisotropic and isotropic mesh adaption procedure with the same accuracy (first row) and number of elements (second row) for test case $E1$.

| | Anisotropic | Isotropic |
|---|---|---|
| $\|\|\|e_h\|\|\| \simeq 0.33$ | 7.86 | 108 |
| $\sharp\mathcal{T}_h = 2500$ | 83.4 | 68.8 |

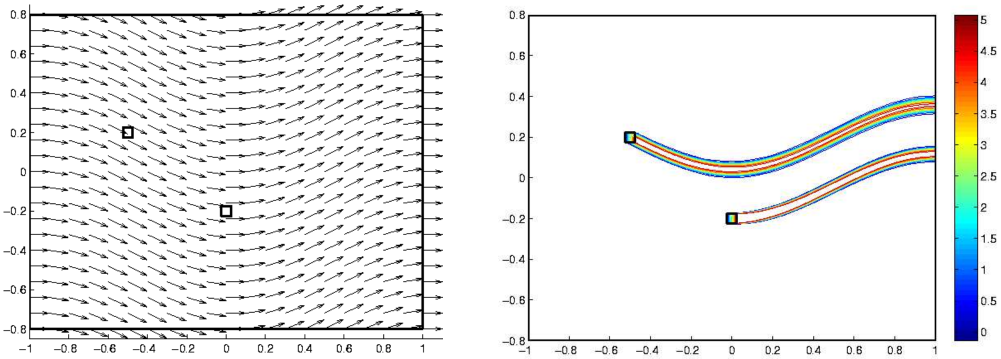

Figure 7: Advective field (left) and contour-lines of the reference solution (right) for test case $E2$.

the shorter CPU time of the anisotropic adaptive procedure is clearly due to the much lower number of elements at hand. On the other hand with the same number of elements the anisotropic procedure is slightly more expensive: this is no surprise, since the anisotropic error estimator involves the discretization error $e_h$ in its definition, this requiring an overhead due to the ZZ recovery procedure.

*Test case $E2$: the "two chimney" case.*

We now deal with a problem motivated by a real environmental issue. In particular, we want to study the diffusion and the transport of a pollutant emitted in air by industrial chimneys in the presence of strong wind (see also [9, 29] for an optimal control approach in this application).

For this test case we choose in (1) $\mu = 10^{-3}$, $\mathbf{b} = (1, 0.5\sin(\pi x_1))^T$, $\gamma = 0$, $\Omega = (-1,1) \times (-0.8, 0.8)$, $\Gamma_D = \{x_1 = -1\}$, $g = 0$ and $f = 100\chi_{E_1 \cup E_2}$, where $\chi_{E_i}$ is the characteristic function associated with the emission area $E_i$, with $i = 1, 2$, $E_i$ being the squared subdomains centered at $(-0.5, 0.2)$ and $(0, -0.2)$, respectively, with side equal to 0.05. Figure 7 displays the advective flow field (left) along with the reference solution (right) computed on a sufficiently fine uniform grid.

In Fig. 8 we contrast the meshes yielded by the anisotropic (left) and isotropic

Memory Cache and 256 MB of RAM.

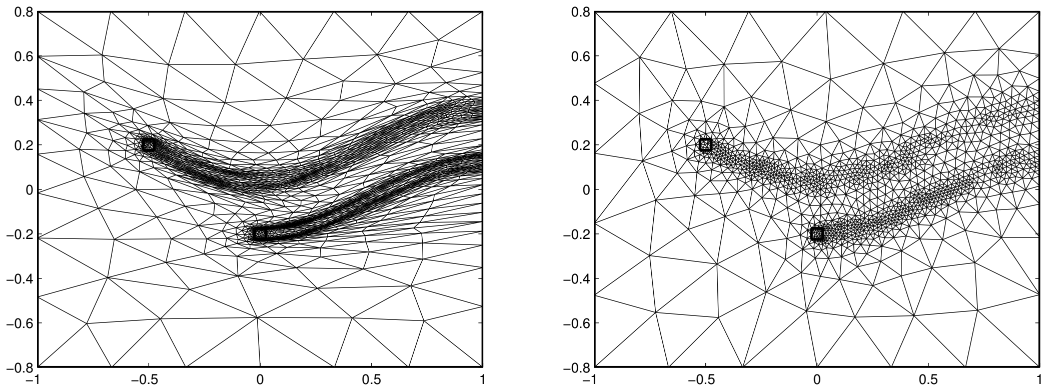


Figure 8: Anisotropic (left) versus isotropic (right) adapted mesh with the same number of elements (2300) for test case $E2$.

(right) adaptive procedure with the same number of triangles, i.e. 2300. By comparing Fig. 8 with 7 it is easily seen that both the adapted meshes detect the pollutant wakes. However it is also evident that the anisotropic grid fits more accurately all the internal layers characterizing the reference solution. In fact, zooming on the lower chimney (see Fig. 9), it can be appreciated the "coarsening" in the middle of the wake in the anisotropic case completely absent in the isotropic mesh. Note also that the misleading uniform distribution of the elements in the isotropic case is actually due to the small dimension of the zoom box.
The better accuracy of the anisotropic approximation is further corroborated by the contour-lines in Fig. 10, compact in the anisotropic case while scattered on the isotropic mesh. Also remarkable is the accuracy of the anisotropic solution inside the emission area.

# 6 The goal-oriented anisotropic analysis

In view of environmental applications one may be interested in accurately approximating physically relevant quantities such as, for instance, concentrations around critical areas of the domain, or fluxes across sections of interest. These goal quantities can be mathematically represented by suitable linear (or nonlinear) functional $J$ of the solution. The goal-oriented framework fully fits this need ([3, 16]). The merging of this approach with the anisotropic framework has already been carried out for the ADR equation and also the Stokes problem [11, 14].
In this section after deriving an error estimate equivalent, up to a constant, to the one in [11], we provide an alternative approach for the case of a linear $J$ preserving the nice feature of the estimate (24) to depend on the error, i.e. to likely converge at a faster rate.
The main ingredient of the goal-oriented analysis is the introduction of an auxil-

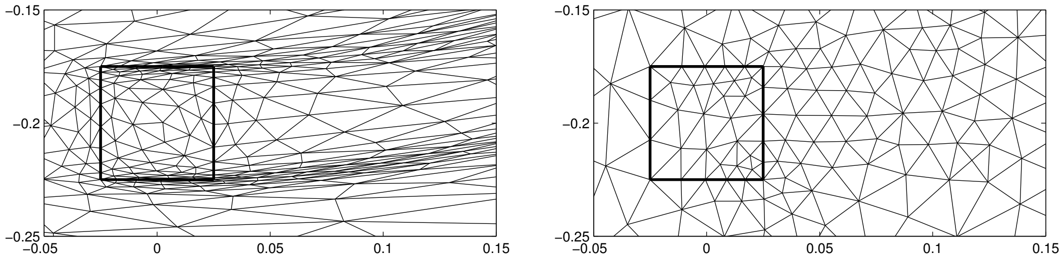


Figure 9: Detail of the anisotropic (left) versus isotropic (right) adapted mesh around the lower chimney for test case $E2$.

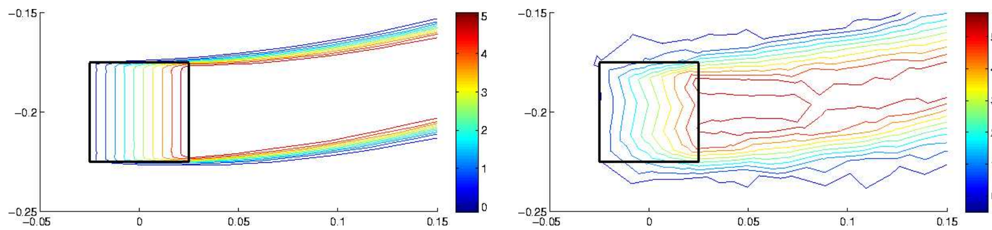


Figure 10: Contour-lines around the lower chimney on the anisotropic (left) and isotropic (right) grid for test case $E2$.

iary problem, the so-called adjoint (or dual) problem related to the functional $J$ at hand. Let $J : V \longrightarrow \mathbb{R}$ be the linear goal functional. Thus the dual problem associated with the ADR (primal) problem (2) reads:

$$\text{find } z \in V \ : \ B_h(v, z) = J(v) \quad \forall v \in V, \tag{49}$$

the stabilized bilinear form $B_h(\cdot, \cdot)$ being defined in (6). The corresponding discrete problem is

$$\text{find } z_h \in V_h \ : \ B_h(v_h, z_h) = J(v_h) \quad \forall v_h \in V_h. \tag{50}$$

A first anisotropic bound on the functional $J(e_h)$ of the discretization error can now be stated.

**Proposition 6.1** *Let $u$, $z \in V$ be the solutions of the primal and dual problems* (2) *and* (49)*, respectively, and $u_h$, $z_h \in V_h$ be the corresponding approximations satisfying* (5) *and* (50)*, respectively. Moreover, let us assume that $u$ is smooth enough such that the standard Galerkin orthogonality* (9) *holds. Then the following estimate can be proved,*

$$|J(e_h)| \leq C \sum_{K \in \mathcal{T}_h} \alpha_K \rho_K(u_h) w_K(z), \tag{51}$$

*with $C = C(N, C_\Delta)$, $\alpha_K$, $\rho_K(u_h)$ defined as in Proposition 4.1, while*

$$w_K(z) = \left[ s_K \left( \mathbf{r}_{1,K}^T G_K(z) \mathbf{r}_{1,K} \right) + \frac{1}{s_K} \left( \mathbf{r}_{2,K}^T G_K(z) \mathbf{r}_{2,K} \right) \right]^{1/2}.$$

**Proof.** By suitably combining the dual formulation (49) together with the Galerkin orthogonality (9), the definitions of $B_h(\cdot,\cdot)$ in (6) and of the strong form of the ADR equation in (1), we get

$$\begin{aligned} J(e_h) &= B_h(e_h, z) = B_h(e_h, z - v_h) \\ &= B(e_h, z - v_h) + \sum_{K \in \mathcal{T}_h} \tau_K \left( r_K(u_h), \mathbf{b} \cdot \nabla (z - v_h) \right) \quad \forall v_h \in V_h. \end{aligned} \tag{52}$$

Using (29) with $v = z - v_h \in V$, we have:

$$\begin{aligned} J(e_h) = \sum_{K \in \mathcal{T}_h} \Bigg\{ & \int_K r_K(u_h)(z - v_h)\, d\Omega + \frac{1}{2} \int_{\partial K} j_K(u_h)(z - v_h)\, d\Gamma \\ & + \tau_K \int_K r_K(u_h) \mathbf{b} \cdot \nabla (z - v_h)\, d\Omega \Bigg\}. \end{aligned} \tag{53}$$

Using the Cauchy-Schwarz inequality, the functional of the error can be bounded as

$$\begin{aligned} |J(e_h)| \le \sum_{K \in \mathcal{T}_h} \Bigg\{ & \|r_K(u_h)\|_{L^2(K)} \Big[ \|z - v_h\|_{L^2(K)} + \tau_K \|\mathbf{b}\|_{L^\infty(K)} |z - v_h|_{H^1(K)} \Big] \\ & + \frac{1}{2} \|j_K(u_h)\|_{L^2(\partial K)} \|z - v_h\|_{L^2(\partial K)} \Bigg\} \quad \forall v_h \in V_h. \end{aligned} \tag{54}$$

The choice $v_h = I_h^1 z \in V_h$ together with Proposition 3.1 leads us to the final result (51), $C$ coinciding now with the maximum of the interpolation constants $C_1$, $C_2$, $C_3$ in Proposition 3.1. $\diamond$ $\square$

**Remark 6.1** *The use of the stabilized dual weak form (49), at variance with [11], is justified in view of Proposition 6.2. The same kind of estimate is obtained in both cases, the only change consisting of a different value for the constant $C$ in (51), with $C = \max(C_1, 1 + C_2, C_3)$ in [11].*

As in the case of Proposition 4.1 the right-hand side of (51) cannot be used yet as an a posteriori error estimator, the exact adjoint solution $z$ being in general unknown. An actual estimator can be obtained via the following

**Definition 6.1** *Let $u_h$, $z_h \in V_h$ be the solutions of the discrete problems (5) and (50), respectively. Then the error on the functional $J$ can be estimated by the quantity*

$$\eta^{J_1} = \sum_{K \in \mathcal{T}_h} \eta_K^{J_1}, \tag{55}$$

*$\eta_K^{J_1}$ being the local error indicator given by*

$$\eta_K^{J_1} = \alpha_K \rho_K(u_h) w_K(z^*) \tag{56}$$

*where $\alpha_K$ and $\rho_K(u_h)$ are still defined as in Proposition 4.1, while*

$$w_K(z^*) = \left[ s_K \left( \mathbf{r}_{1,K}^T G_K(z^*) \mathbf{r}_{1,K} \right) + \frac{1}{s_K} \left( \mathbf{r}_{2,K}^T G_K(z^*) \mathbf{r}_{2,K} \right) \right]^{1/2}, \tag{57}$$

*$G_K(z^*)$ being computed relying on the ZZ recovery procedure applied to $z_h$.*

We have now all the tools necessary to introduce the variant of the estimator $\eta^{J_1}$, hopefully enjoying better approximation properties.

**Proposition 6.2** *An estimate alternative to* (51) *for the functional of the discretization error is provided by the relation*

$$|J(e_h)| \leq C \sum_{K \in \mathcal{T}_h} \alpha_K \rho_K(u_h) w_K(e_z), \tag{58}$$

$e_z = z - z_h$ *being the dual discretization error and with*

$$w_K(e_z) = \left[ s_K \left( \mathbf{r}_{1,K}^T G_K(e_z) \mathbf{r}_{1,K} \right) + \frac{1}{s_K} \left( \mathbf{r}_{2,K}^T G_K(e_z) \mathbf{r}_{2,K} \right) \right]^{1/2}. \tag{59}$$

**Proof.** Result (58) follows simply by mimicking the proof of Proposition 6.1 choosing in the end $v_h = z_h + I_h^1(z - z_h)$. $\diamond$ $\square$ Analogously to estimate (24) the weight of the right-hand side of (58) depends on the unknown error, in this case the dual one. We follow the same approach as in Section 4 (see (35)) where the matrix $G_K(e_z)$ in the definition of $w_K(e_z)$ is replaced by the matrix of the recovered gradients $G_K(e_z^*)$ given by

$$[G_K(e_z^*)]_{i,j} = \sum_{T \in \Delta_K} \int_T \left( (\nabla^{ZZ} z_h)_i - \frac{\partial z_h}{\partial x_i} \right) \left( (\nabla^{ZZ} z_h)_j - \frac{\partial z_h}{\partial x_j} \right) d\Omega, \tag{60}$$

for $i, j = 1, 2$. The fully computable estimator for $J(e_h)$ is provided in

**Definition 6.2** *With the same notations as in Definition* 6.1*, the global anisotropic a posteriori error estimator for the functional of the discretization error* $e_h$ *is*

$$\eta^{J_2} = \sum_{K \in \mathcal{T}_h} \eta_K^{J_2}, \tag{61}$$

$\eta_K^{J_2}$ *being the local error indicator given by*

$$\eta_K^{J_2} = \alpha_K \rho_K(u_h) w_K(e_z^*), \tag{62}$$

*the weight* $w_K(e_z^*)$ *being*

$$w_K(e_z^*) = \left[ s_K \left( \mathbf{r}_{1,K}^T G_K(e_z^*) \mathbf{r}_{1,K} \right) + \frac{1}{s_K} \left( \mathbf{r}_{2,K}^T G_K(e_z^*) \mathbf{r}_{2,K} \right) \right]^{1/2}. \tag{63}$$

# 7 Goal-oriented analysis: numerical assessment

This section replies Section 5 in the goal-oriented framework and with reference to the estimators (55) and (61). In particular, due to the similar structure of the estimator (36) with the new ones $\eta^{J_1}$ and $\eta^{J_2}$, the description of the adaptive procedure is here kept to a minimum.

## 7.1 The adaptive procedure

The procedure employed to derive the constrained minimization problem (44) can be mimicked also for the goal-oriented estimators (55) and (61). The substantial differences are essentially two: the new definition of the objective function $I(s_K, \mathbf{r}_{1,K})$ involves the scaled matrices $\widetilde{G}_K(z^*)$ and $\widetilde{G}_K(e_z^*)$ instead of the matrix $\widetilde{G}_K(e_h^*)$; then notice that the local estimators (56) and (62) do not entail any square root in contrast to the local estimator (37). The analogue of Proposition 5.1 can thus be stated

**Proposition 7.1** *The optimal metric $\widetilde{M}$ is identified by the following choices:*

$$\widetilde{\lambda}_{1,K} = \sqrt{\widetilde{s}_K q}, \qquad \widetilde{\lambda}_{2,K} = \sqrt{\frac{q}{\widetilde{s}_K}}, \qquad \widetilde{\mathbf{r}}_{1,K} = \mathbf{p}_{2,K},$$

*where*

$$\widetilde{s}_K = \sqrt{\frac{\sigma_{1,K}}{\sigma_{2,K}}}, \qquad q = \left[ \frac{\tau^2}{|\widehat{K}|^2 (\widetilde{\rho}_K(u_h))^2 \, (\widetilde{s}_K \sigma_{2,K} + \sigma_{1,K}/\widetilde{s}_K)} \right]^{1/3},$$

*$\sigma_{1,K}$ and $\sigma_{2,K}$ are the maximum and the minimum eigenvalues of the matrix $\widetilde{G}_K(z^*)$ or $\widetilde{G}_K(e_z^*)$ according to the choice $\eta^{J_1}$ or $\eta^{J_2}$, respectively and with $\mathbf{p}_{i,K}$ the corresponding eigenvectors.*

The adaptive algorithm detailed in Section 5.1 will be exploited as is in the numerical validation below.

## 7.2 Numerical tests

In the following we compare the performances of the estimators $\eta^{J_1}$ and $\eta^{J_2}$ on three test cases, the first one purely academic, the others being instead aimed at environmental applications. In particular, as we are dealing with a goal-oriented approach, the linear functional $J(\cdot)$ in (49) will be chosen on the basis of environmental motivations.

*Test case $G1$: the "ramp" case.*

We come back to the test case $E1$ in Section 5.2, now reviewed in a goal-oriented setting. The target functional is $J(u) = \int_D u \, d\Omega = 0.2741$, $D$ being the rectangle with coordinates $(3, 0.9)$, $(4, 0.9)$, $(4, 1)$ and $(3, 1)$ (see the boxed area in the top-right corner of Fig. 11). The corresponding dual solution is displayed in Fig. 11: as the dual source term involves a localized quantity and the problem is strongly advective dominated, the dual solution is confined to the upper horizontal slab of the domain, i.e. the region feeding the information into the region $D$. In Fig. 12 we show the anisotropic grids driven by the estimators $\eta^{J_1}$ (left) and $\eta^{J_2}$ (right), sharing the same number of triangles (about 1600). A qualitative comparison among these meshes and the anisotropic ones in Fig. 4 and 3 highlights the significant role played by the functional $J$ in the goal-oriented case: the three boundary layers exhibited by the primal solution are no longer detected, while only the region carrying information towards the rectangle $D$ is refined. A suitable zoom of the meshes in Fig. 12 in correspondence with the top side of

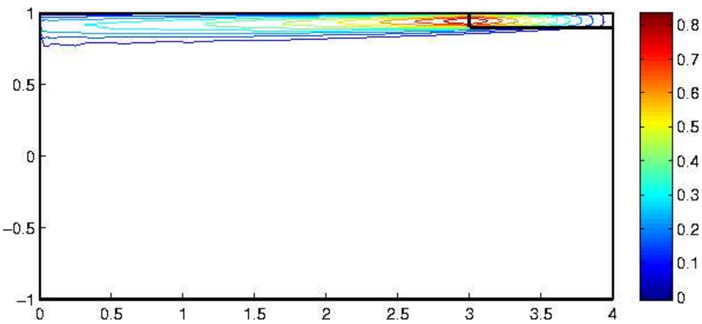


Figure 11: Contour-lines of the adjoint solution for test case $G1$.

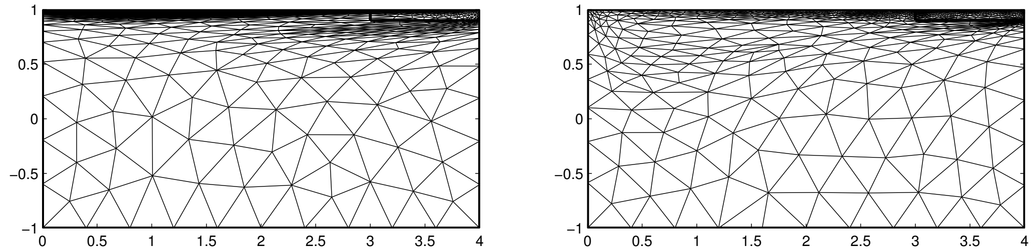

Figure 12: Anisotropic adapted mesh driven by $\eta^{J_1}$ (left) versus $\eta^{J_2}$ (right) with the same number of elements (1600) for test case $G1$.

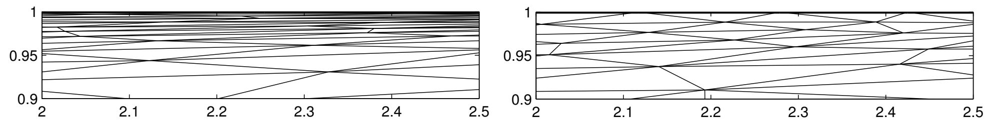

Figure 13: Zooms of the meshes in Fig. 12 associated with $\eta^{J_1}$ (left) and $\eta^{J_2}$ (right) for test case $G1$.

the domain is provided in Fig. 13. The two details emphasize the less anisotropic exasperated nature of the mesh identified by the estimator (61). This is to be expected due to the dependence of the matrix $G_K$ on the dual error rather than on the dual solution.
Finally, we compare the convergence histories associated with $\eta^{J_1}$, $\eta^{J_2}$ and the isotropic counterpart of $\eta^{J_2}$, i.e. $\eta^{J_2}_{iso}$ (see [3] for an instance of the corresponding recipe). As Fig. 14 demonstrates, the anisotropic estimator (61) exhibits a faster convergence compared with both $\eta^{J_1}$ and $\eta^{J_2}_{iso}$. This implies a lower number of triangles in order to guarantee a given accuracy or, likewise, a higher accuracy

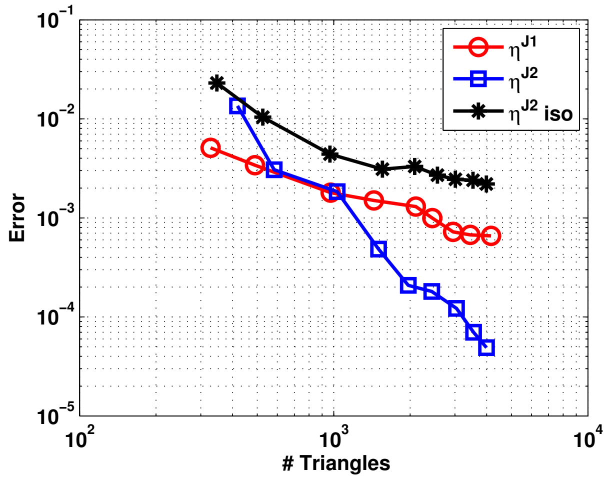


Figure 14: Convergence histories associated with the anisotropic estimators $\eta^{J_1}$ (O), $\eta^{J_2}$ ($\Box$) and the isotropic estimator $\eta^{J_2}_{iso}$ ($*$) for test case $G1$.

for a fixed number of d.o.f.'s.

*Test case $G2$: the "channel" case.*

This test case deals with an environmental problem modeling transport of pollution in water. In particular, two pollutant sources $E_1$ and $E_2$ are placed in a river characterized by a dry area (an island, for example) localized in the center of the domain. Our aim is the evaluation of the average value of the pollutant concentration in a zone $D$ of interest (e.g., a fish or beach area). Figure 15 (left) sketches this setting. With reference to the ADR equation (1), the advective field $\mathbf{b}$ (see Fig. 15, right) is computed by solving the incompressible Navier-Stokes equations with the following data: the Reynolds number is chosen equal to 100, a parabolic inflow profile with average value 1 is enforced at the inflow boundary $\{x_1 = 0\}$, while a no slip condition holds on the land borders and a homogeneous Neumann condition is assigned at the outflow $\{x_1 = 8\}$. As far as the other data of equation (1) is concerned, we take $\mu = 10^{-3}$, $\gamma = 0$, $\Gamma_D = \{x_1 = 0\}$ and the source term $f = 100\,\chi_{E_1 \cup E_2}$. Finally the output functional is $J(u) = \int_D u\, d\Omega$. As reference solution we choose the approximation computed on a uniform mesh with 51008 triangles, thus the goal value being equal to 1.2355. The contour-lines of the primal and dual solutions are displayed in Fig. 16, left and right, respectively. We can appreciate that only the emission area $E_1$ influences the zone of interest $D$ as a consequence of the strong horizontal advective field (notice also the perturbation on the dual solution due to the dry area). This is further confirmed by the adaptive grids yielded by $\eta^{J_1}$ and $\eta^{J_2}$, for a fixed number of elements (about 1500), as shown in Fig. 17 (left and right, respectively). A zoom of the adapted mesh around the emission source $E_1$ is provided in Fig. 18: the grid associated with the estimator $\eta^{J_1}$ is clearly the most anisotropic one. Finally, concerning the converge history, similar conclusions as in Fig. 14 can be drawn (see Fig. 19).

*Test case $G3$: the "PIT tag detection" case.*

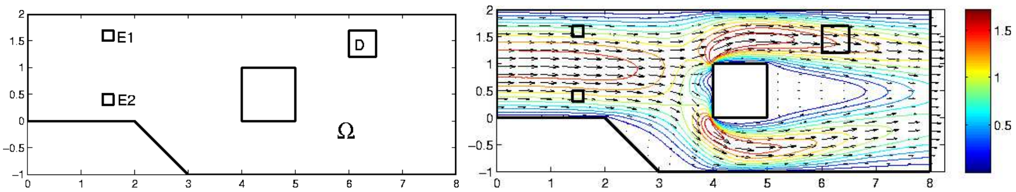


Figure 15: Domain (left) and advective field **b** (right) for test case $G2$.

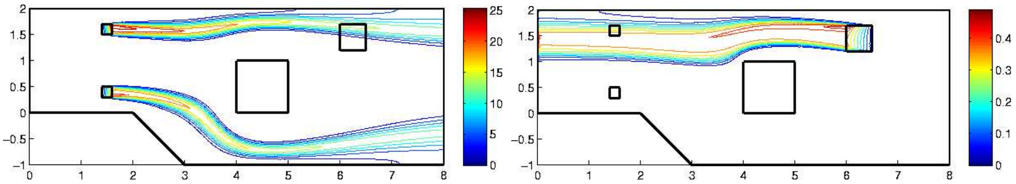

Figure 16: Contour-lines for the primal (left) and dual (right) solution for test case $G2$.

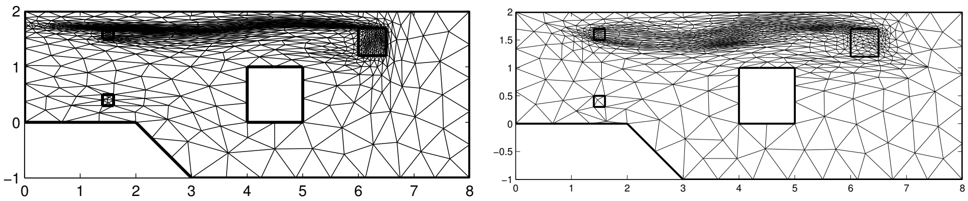

Figure 17: Anisotropic adapted mesh driven by $\eta^{J_1}$ (left) versus $\eta^{J_2}$ (right) with the same number of elements (1500) for test case $G2$.

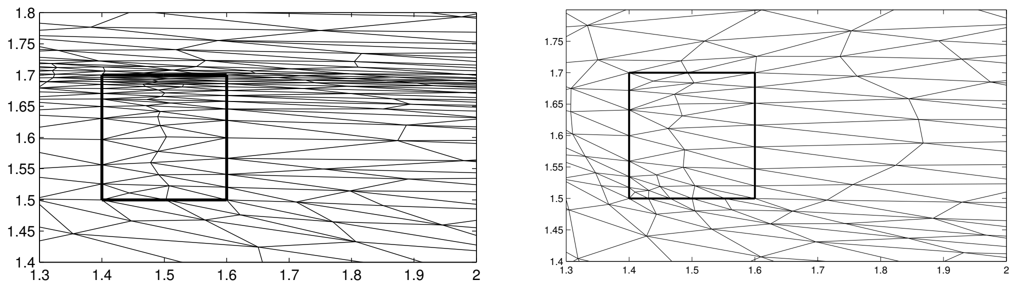

Figure 18: Zooms of the meshes in Fig. 17 associated with $\eta^{J_1}$ (left) and $\eta^{J_2}$ (right) for test case $G2$.

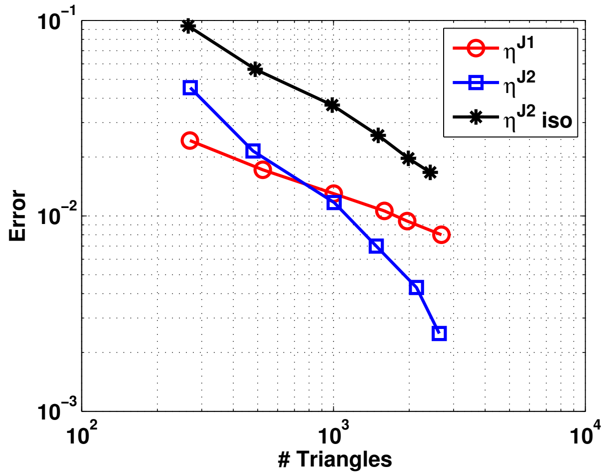


Figure 19: Convergence histories associated with the anisotropic estimators $\eta^{J_1}$ (O), $\eta^{J_2}$ (□) and the isotropic estimator $\eta^{J_2}_{iso}$ ($*$) for test case $G2$.

This test case can be regarded as an environmental problem concerning with Radio Frequency IDentification (RFID) of animals. In particular we deal with a PIT (Passive Integrated Transponder) technology providing a variety of identification and monitoring solutions for fish and wildlife research (see e.g., [31]). PIT tags have been used for over twenty years to permanently identify individual animals. The small size of PIT tags, also known as "microchips", virtually eliminates negative impact on animals with little or no influence on growth-rate, behavior or health, and makes recapture unnecessary, thus reducing handling time and stress to the animal. The principle of RFID is to use a signal transmitted between an electronic device, such as a "tag", "transponder" or "microchip" and a reading device, such as a "scanner", "reader" or "transceiver". The RFID or EID (Electronic IDentification) devices most widely used in animals are passive. Passive integrated transponders have no battery so the microchip remains inactive until read with a scanner. The scanner sends a low frequency signal to the microchip within the tag providing the power needed to send its unique code back to the scanner and positively identify the animal.

In our test case we simulate a typical monitoring situation in the case of fishes, under the 2D approximation that the vertical motion of the fishes is negligible. Suppose that a school of fishes are PIT tagged and then continuously released in a small area off sea. We are then interested in measuring the fish flux across a rectangular creel located downwind a strong eddy. We also assume that the phenomenon takes place in an area whose size is large compared with the dimension of the fishes so that the fish random motion by "diffusion" is dominated by the convective effects. We model the fish evolution by the steady ADR equation (1). The domain $\Omega = (-1, 1)^2$ is reported in Fig. 20 (left), along with the dump area $E$ and the creel $(-0.05, 0.05) \times (-1, 0)$. The advective field $\mathbf{b}$ is approximated by the elliptic contracting spiral

$$\mathbf{b} = (b_1, b_2)^T = (x_2 - 0.1x_1, 3(-x_1 - 0.1x_2))^T , \tag{64}$$

with $\nabla \cdot \mathbf{b} = -0.4$, and the corresponding flow field is shown in Fig. 20 (right). As for the other data of the ADR equation (1), we take $\mu = 10^{-3}$, $\gamma = 0$, $f = 100\chi_E$, $E$ being the squared release area of side 0.1 centered at (0.5,0.5), and $\Gamma_N = \emptyset$.
The goal functional is given by $J(u) = -\int_{\text{Creel}} b_1 u \, d\Omega \simeq 7.885 \cdot 10^{-2}$, as approximated on a uniform fine grid consisting of 86144 elements.

The color plots of the reference primal and adjoint solutions are displayed

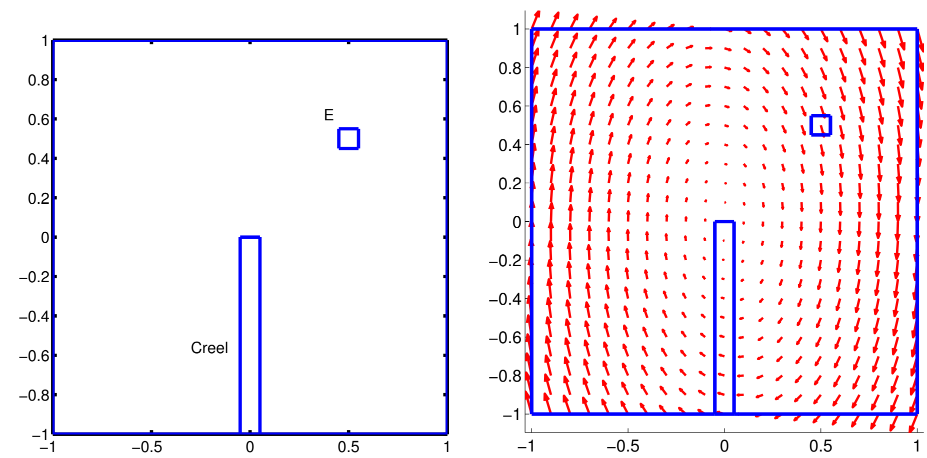


Figure 20: Domain (left) and advective flow field (right) for test case $G3$.

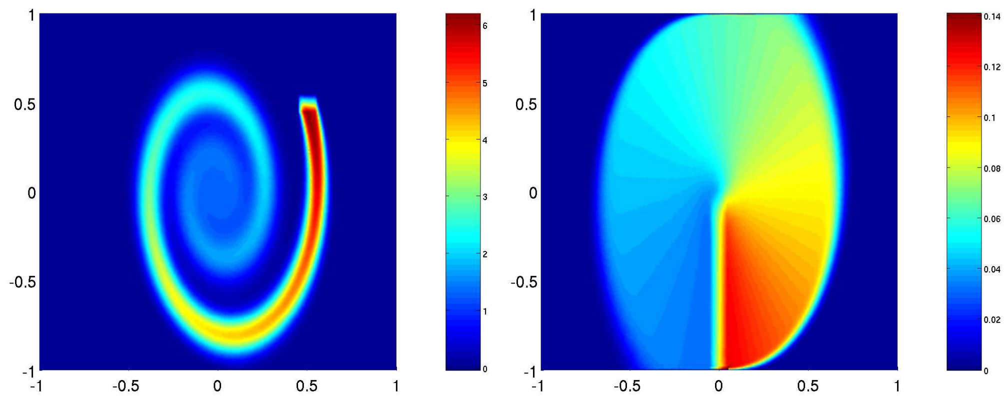

Figure 21: Color plot of the primal (left) and adjoint (right) reference solutions for test case $G3$.

in Fig. 21 (left) and (right), respectively. In Fig. 22 we show the anisotropic adapted mesh, with about 1250 triangles, obtained by means of the estimators $\eta^{J_1}$ (left) and $\eta^{J_2}$ (right). Both the meshes highlight the regions mostly affecting the computation of the output functional $J$ according to the interplay between the primal and the adjoint solutions. In particular, as shown in Fig. 22, the dual solution provides us with a qualitative information by selecting the area involved in the adaptivity. On the other hand, the details of the mesh inside this area

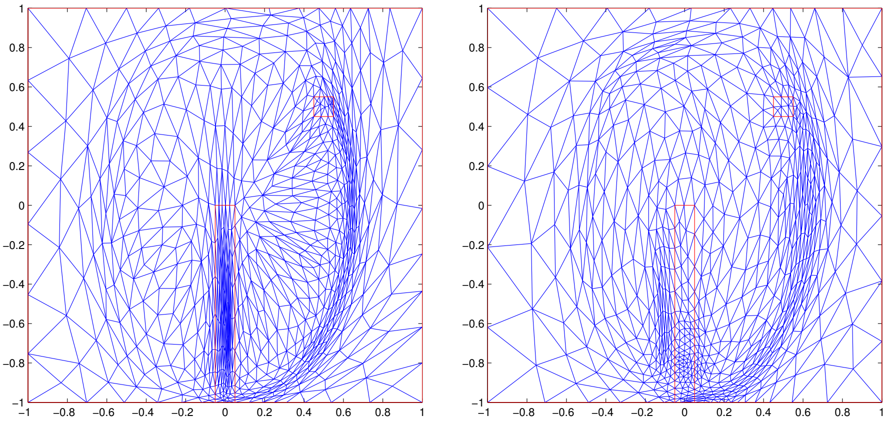


Figure 22: Anisotropic adapted mesh driven by $\eta^{J_1}$ (left) and $\eta^{J_2}$ (right) with the same number of elements (1250) for test case $G3$.

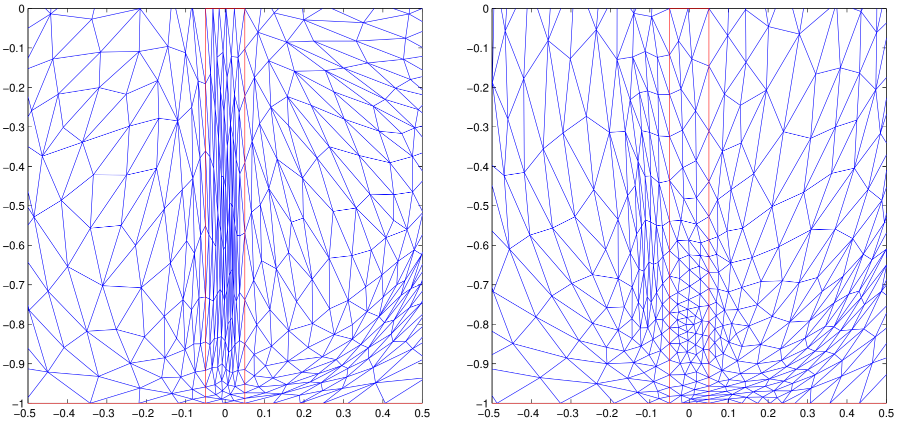


Figure 23: Zooms around the creel of the meshes in Fig. 22 associated with $\eta^{J_1}$ (left) and $\eta^{J_2}$ (right) for test case $G3$.

are due to both the strong gradients of the dual solution and to the intensity of the primal solution which gets lower and lower as we move towards the center of the domain (see Fig. 21). Both the estimators detect the same critical area by placing anisotropic triangles along the primal streamline, though the layers associated with $\eta^{J_2}$ are larger than the ones corresponding to $\eta^{J_1}$. Notice also that the orientation of the triangles around the center of the domain is quite different.

Figure 23 provides zooms around the creel of the adapted meshes of Fig. 22. Observe the crowding and the strong anisotropic features of the triangles yielded by $\eta^{J_1}$ (on the left) due to the large gradient of the adjoint solution in that area. On the other hand the estimator $\eta^{J_2}$, depending on the gradient of the error of the adjoint solution, exhibits less apparent anisotropic characteristics.

In Fig. 24 we gather the convergence histories associated with the estimators

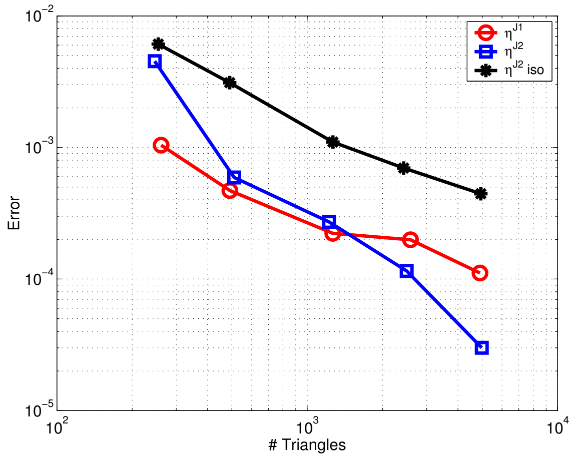


Figure 24: Convergence histories associated with the anisotropic estimators $\eta^{J_1}$ (O), $\eta^{J_2}$ ($\square$) and the isotropic version of estimator $\eta^{J_2}$, $\eta^{J_2}_{iso}$, ($*$) for test case $G3$.

$\eta^{J_1}$, $\eta^{J_2}$ and $\eta^{J_2}_{iso}$. The same type of conclusions as in the previous test cases can be inferred: the estimator $\eta^{J_2}$ allows for a better convergence rate with respect to $\eta^{J_1}$. The isotropic version of the estimator $\eta^{J_2}$, i.e., $\eta^{J_2}_{iso}$, leads to errors larger than those yielded by $\eta^{J_1}$ and $\eta^{J_2}$, for a fixed number of elements, or equivalently, to a saving of d.o.f's when the same tolerance is considered.

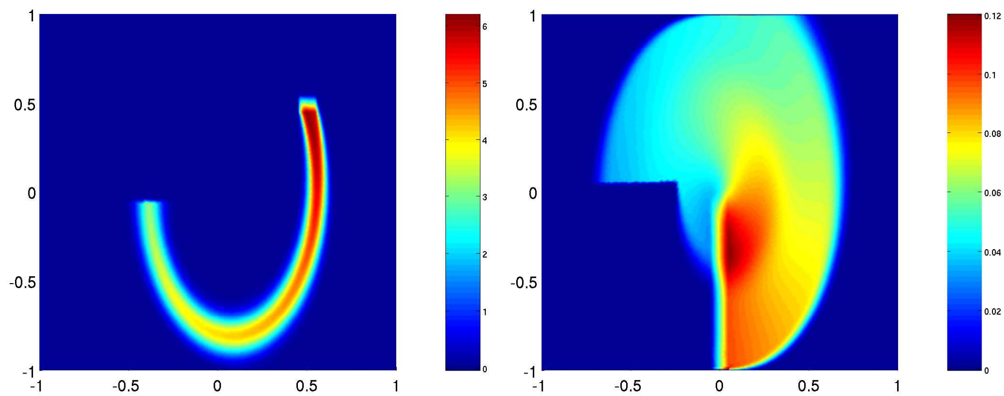

Figure 25: Color plot of the primal (left) and adjoint (right) reference solutions for test case $G3$ with fishing.

We now consider a variant of the previous test case in which we include the effect of a strong (and possibly fraudulent) fishing activity taking place downwind the monitoring region. We model this phenomenon by adding a reaction term $\gamma$ of value 100 in the region $F = (-1, -0.25) \times (-0.05, 0.05)$. The color plots of the reference primal and adjoint solutions, computed on the same fine mesh as above, are shown in Fig. 25 (left) and (right), respectively. Note the "barrier" effect due to the presence of the fishing area. The goal functional is still $J(u) = -\int_{\text{Creel}} b_1 u \, d\Omega \simeq 6.057 \cdot 10^{-2}$, which is slightly lower than the previous

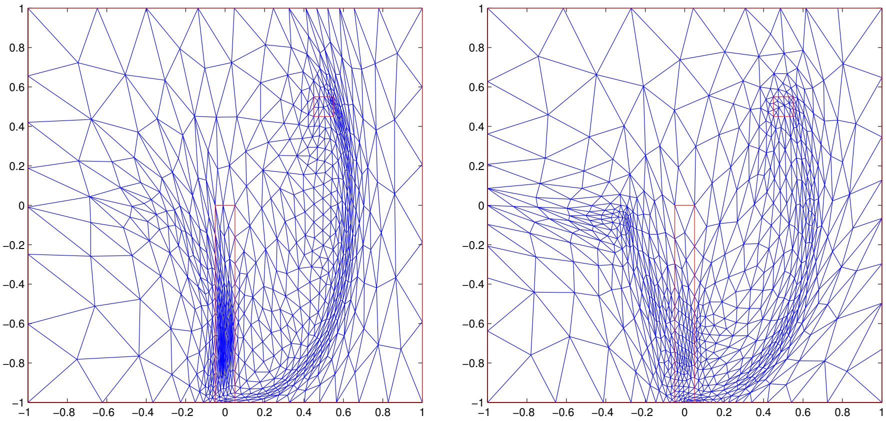


Figure 26: Anisotropic adapted mesh driven by $\eta^{J_1}$ (left) and $\eta^{J_2}$ (right) with the same number of elements (1250) for test case $G3$ with fishing.

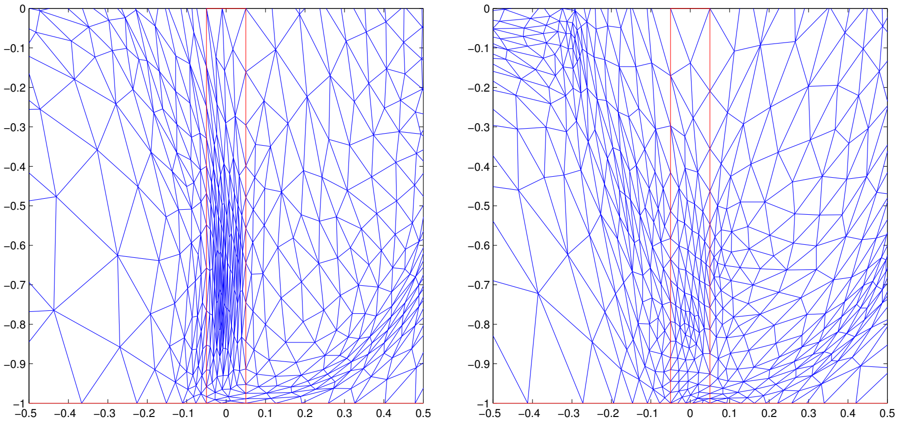


Figure 27: Zooms of the meshes in Fig. 26 associated with $\eta^{J_1}$ (left) and $\eta^{J_2}$ (right) for test case $G3$ with fishing.

case due the capture of fishes. In Fig. 26 we provide the anisotropic adapted meshes, with about 1250 triangles, associated with the estimators $\eta^{J_1}$ (left) and $\eta^{J_2}$ (right). On comparing Fig. 22 with Fig. 26, the most striking evidence is that in the left and top parts of the domain the grid is not refined as the fishing activity is actually interrupting the flow. Moreover, the refinement localized along the region $F$ in Fig. 26 (right) is maybe due to a poor approximation of the dual solution $z$. Figure 27 details the adapted meshes in Fig. 26 around the creel. As in Fig. 23, it is apparent the more anisotropic nature of the grid associated with $\eta^{J_1}$. In Fig. 28 we plot the convergence histories corresponding to the estimators $\eta^{J_1}$, $\eta^{J_2}$ and $\eta^{J_2}_{iso}$. Similar conclusions as in the previous test cases hold.

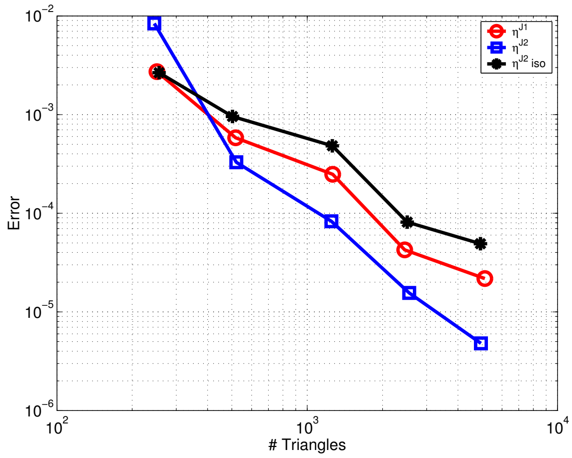


Figure 28: Convergence histories associated with the anisotropic estimators $\eta^{J_1}$ (O), $\eta^{J_2}$ ($\square$) and the isotropic version of estimator $\eta^{J_2}$, $\eta^{J_2}_{iso}$, ($*$) for test case $G3$ with fishing.

# 8 Conclusions

We have shown via some basic test cases that an a posteriori driven anisotropic mesh adaption procedure can be effective in tackling environmental applications modeled by the ADR equation (1), especially in the presence of strong advective fields. In more detail, for a desired accuracy the CPU time reduces considerably due to the lower number of elements required by the anisotropic procedure. In addition, the combined use of anisotropic adaption together with a goal-oriented analysis turns out to be resolvent in view of the monitoring of quantities of physical interest in environmental applications. The natural successive step will lead us to an anisotropic optimal control approach.

# References


[1] T. Apel, Anisotropic Finite Elements: Local Estimates and Applications, Advances in Numerical Mathematics, Teubner, Stuttgart, 1999.

[2] W. Bangerth and R. Rannacher, Adaptive Finite Element Methods for Differential Equations, Birkhauser Verlag, Basel, 2003.

[3] R. Becker and R. Rannacher, An optimal control approach to a posteriori error estimation in finite element methods, Acta Numer. 10 (2001) 1–102.

[4] A.N. Brooks and T.J.R. Hughes, Streamline upwind/Petrov–Galerkin formulations for convection dominated flows with particular emphasis on the incompressible Navier–Stokes equations, Comput. Methods Appl. Mech. Engrg. 32 (1–3) (1982) 199–259.

[5] M.J. Castro–Díaz, F. Hecht, B. Mohammadi and O. Pironneau, Anisotropic unstructured mesh adaption for flow simulations, Internat. J. Numer. Methods Fluids 25 (4) (1997) 475–491.

[6] Ph.G. Ciarlet, The Finite Element Method for Elliptic Problems, North–Holland, Amsterdam, 1978.

[7] Ph. Clément, Approximation by finite element functions using local regularization, RAIRO Anal. Numér. 2 (1975) 77–84.

[8] D.L. Darmofal and D.A. Venditti, Grid adaption for functional outputs: application to two–dimensional inviscid fluids, J. Comput. Phys. 176 (1) (2002) 40–69.

[9] L. Dedè and A. Quarteroni, Optimal control and numerical adaptivity for advection–diffusion equations, M2AN Math. Model. Numer. Anal. 39 (5) (2005) 1019–1040.

[10] G. Finzi, M. Pirovano and M. Volta, Gestione della Qualità dell'Aria. Modelli di Simulazione e Previsione, Mc Graw–Hill, Milano, 2001.

[11] L. Formaggia, S. Micheletti and S. Perotto, Anisotropic mesh adaptation in computational fluid dynamics: application to the advection–diffusion–reaction and the Stokes problems, Appl. Numer. Math. 51 (2004) 511–533.

[12] L. Formaggia and S. Perotto, New anisotropic a priori error estimates, Numer. Math. 89 (2001) 641–667.

[13] L. Formaggia and S. Perotto, Anisotropic error estimates for elliptic problems, Numer. Math. 94 (2003) 67–92.

[14] L. Formaggia, S. Perotto and P. Zunino, An anisotropic a–posteriori error estimate for a convection-diffusion problem, Comput. Vis. Sci. 4 (2) (2001) 99–104.

[15] L. Formaggia and V. Selmin, Simulation of hypersonic flows on unstructured grids, Internat. J. Numer. Methods Engrg. 34 (1992) 569–606.

[16] M.B. Giles and E. Süli, Adjoint methods for PDEs: a posteriori error analysis and postprocessing by duality, Acta Numer. 11 (2002) 145–236.

[17] W.G. Habashi, M. Fortin, J. Dompierre, M.G. Vallet and Y. Bourgault, Anisotropic mesh adaptation: a step towards a mesh–independent and user–independent CFD, in: V. Venkatakrishnan, M.D. Salas, S.R. Chakravarthy (Eds.), Barriers and Challenges in Computational Fluid Dynamics, Kluwer Academic, Dordrecht, 1998 99–117.

[18] F. Hecht, BAMG: bidimensional anisotropic mesh generator, INRIA report (1998), `http://www.inria.fr/`

[19] G. Kunert, A Posteriori Error Estimation for Anisotropic Tetrahedral and Triangular Finite Element Meshes, PhD Thesis, Fakultät für Mathematik der Technischen Universität Chemnitz, 1999.

[20] J.L. Lions and E. Magenes, Non–Homogeneous Boundary Value Problems and Applications, vol. I, Springer–Verlag, Berlin, 1972.

[21] G. Maisano, S. Micheletti, S. Perotto and C.L. Bottasso, On some new recovery based a posteriori error estimators, Comput. Methods Appl. Mech. Engrg. 195 (37–40) (2006) 4794–4815.

[22] S. Micheletti and S. Perotto, An anisotropic recovery-based aposteriori error estimator, in: F. Brezzi, A. Buffa, S. Corsaro, A. Murli (Eds.), Numerical Mathematics and Advanced Applications – ENUMATH2001, Proceedings of the 4th European International Conference on Numerical Mathematics and Advanced Applications, Springer Verlag Italia, 2003 731–741.

[23] S. Micheletti and S. Perotto, Reliability and efficiency of an anisotropic Zienkiewicz–Zhu error estimator, Comput. Methods Appl. Mech. Engrg. 195 (9–12) (2006) 799–835.

[24] S. Micheletti, S. Perotto and M. Picasso, Stabilized finite elements on anisotropic meshes: a priori error estimates for the advection–diffusion and the Stokes problems, SIAM J. Numer. Anal. 41 (3) (2003) 1131–1162.

[25] J.T. Oden and S. Prudhomme, Goal–oriented estimation and adaptivity for the finite element method, Comput. Math. Appl. 41 (5–6) (2001) 735–756.

[26] J.T. Oden and J.N. Reddy, Variational Methods in Theoretical Mechanics, 2nd ed., Springer, Berlin and Heidelberg, 1983.

[27] J. Peraire, M. Vahadati, K. Morgan and O.C. Zienkiewicz, Adaptive remeshing for compressible flow computations, J. Comput. Phys. 72 (1987) 449–466.

[28] M. Picasso, An anisotropic error indicator based on Zienkiewicz–Zhu error estimator: application to elliptic and parabolic problems, SIAM J. Sci. Comput. 24 (4) (2003) 1328–1355.

[29] A. Quarteroni, G. Rozza, L. Dedè and A. Quaini, Numerical approximation of a control problem for advection–diffusion processes, in: Proceedings of 22nd IFIP TC7 Conference, Turin, 2005, System Modeling and Optimization, Ceragioli et al. (Eds.), Springer, 2006.

[30] R. Rodriguez, Some remark on the Zienkiewicz–Zhu estimator, Numer. Methods Partial Differential Equations 10 (1994) 625–635.

[31] J.M. Roussel, A. Haro and R.A. Cunjak, Field test of a new method for tracking small fishes in shallow rivers using passive integrated transponders, Can. J. Fish. Aquat. Sci. 57 (2000) 1326–1329.

[32] K.G. Siebert, An a posteriori error estimator for anisotropic refinement, Numer. Math. 73 (1996) 373–398.

[33] R. Verfürth, A Review of A Posteriori Error Estimation and Adaptive Mesh–refinement Techniques, Wiley–Teubner, New York, 1996.

[34] O.C. Zienkiewicz and J.Z. Zhu, A simple error estimator and adaptive procedure for practical engineering analysis, Internat. J. Numer. Methods Engrg. 24 (2) (1987) 337–357.

[35] O.C. Zienkiewicz and J.Z. Zhu, The superconvergent patch recovery and a posteriori error estimates. Part 1: the recovery technique, Internat. J. Numer. Methods Engrg. 33 (1992) 1331–1364.

[36] O.C. Zienkiewicz and J.Z. Zhu, The superconvergent patch recovery and a posteriori error estimates. Part 2: error estimates and adaptivity, Internat. J. Numer. Methods Engrg. 33 (1992) 1365–1382.